

RESEARCH ARTICLE

10.1002/2014JC010609

Modeling long-term change of planktonic ecosystems in the northern South China Sea and the upstream Kuroshio Current

Qian P. Li¹, Yanjun Wang¹, Yuan Dong¹, and Jianping Gan²¹South China Sea Institute of Oceanology, Chinese Academy of Sciences, Guangzhou, China, ²Division of Environment, Hong Kong University of Science and Technology, Kowloon, Hong Kong

Key Points:

- Long-term ecosystem dynamics in the NSCS was accurately simulated by the model
- Nutrient transport by turbulent mixing above nitracline but Ekman pumping below
- Failure of diazotroph in the NSCS could be attributed to high nitrate fluxes

Correspondence to:

Q. P. Li,
qianli@scsio.ac.cn

Citation:

Li, Q. P., Y. Wang, Y. Dong, and J. Gan (2015), Modeling long-term change of planktonic ecosystems in the northern South China Sea and the upstream Kuroshio Current, *J. Geophys. Res. Oceans*, 120, 3913–3936, doi:10.1002/2014JC010609.

Received 2 DEC 2014

Accepted 6 MAY 2015

Accepted article online 13 MAY 2015

Published online 1 JUN 2015

Abstract Field studies suggested that the biogeochemical settings and community structures are substantially different between the central Northern South China Sea (NSCS) and the upstream Kuroshio Current (KC). In particular, the water column of KC is characterized by substantially lower nutrients and productivity but higher *Trichodesmium* abundance and nitrogen fixation compared to the NSCS. The mechanism driving the difference of the two marine ecosystems, however, remains inadequately understood. Here, a one-dimensional biogeochemical model was developed to simulate the long-term variability of lower-trophic planktonic ecosystem for two pelagic stations in the NSCS and the KC near the Luzon Strait. The physical model included the vertical mixing driven by air-sea interaction and the Ekman pumping induced by wind stress curl. The biological model was constructed by modifying a nitrogen-based NPZD model with the incorporation of phosphorus cycle and diazotroph nitrogen fixation. After validation by several field data sets, the model was used to study the impact of long-term physical forcing on ecosystem variability in the two distinct stations. Our results suggested that nutrient transport above nitracline during summer was largely controlled by vertical turbulent mixing, while Ekman pumping was important for nutrient transport below the nitracline. Our results also indicated that diazotroph community structure and N₂ fixation in the NSCS and the KC could be strongly influenced by physical processes through the impacts on vertical nutrient fluxes. The disadvantage of diazotroph in the NSCS in compared to the KC during the summer could be attributed to its high nitrate fluxes from subsurface leading to outcompete of diazotrophs by faster growing nondiazotroph phytoplankton.

1. Introduction

The northern South China Sea (NSCS) is one of the world's largest semienclosed marginal seas located in the tropical western Pacific. It is influenced by strong northeast monsoon prevailing in the winter and weak southwest monsoon in the summer. The surface mixed layer of the NSCS is generally deepened during the winter monsoon, leading to a shallower nitracline supporting high productivity [Chen, 2005]. In the summer, adverse currents induced by monsoon forcing, however, result in very low phytoplankton productivity over the entire region of the NSCS. Besides the monsoon forcing, ocean circulation of the NSCS is also modulated by a number of processes including typhoons, tropical cyclones, internal waves, and mesoscale eddies [Metzger, 2003; Wang *et al.*, 2009], which often result in enhanced vertical mixing that bring deep nutrients to the surface to support high new production [Lin *et al.*, 2003; Chen, 2005; Liu *et al.*, 2007]. Wind-induced upwelling including Ekman transport, Ekman pumping, and cross-isobath transport is found responsible for midsummer cooling and thus nutrient upwelling in the coastal regions of the NSCS [Xie *et al.*, 2003; Gan *et al.*, 2009, 2010], with Ekman pumping driven by wind stress curl generally dominant in the large area of the offshore regions supporting nutrients for pelagic phytoplankton production over a longer time scale [Metzger, 2003; Wang and Tang, 2014], similar to that in the offshore California Current Ecosystem [Ryckaczewski and Checkley, 2008; Macias *et al.*, 2012]. A time-series study site of the central NSCS (SEATS) with relatively high stratification but weak winter convection has documented substantially temporal change of carbon and nutrient inventories in the NSCS from intra-annual to decadal time scale [Liu *et al.*, 2002; Wong *et al.*, 2007a], providing a key context for understanding the response of long-term chlorophyll-*a* variations to climate oscillations [Liu *et al.*, 2013].

Through the Luzon Strait, surface water exchange takes place between the NSCS and the western North Pacific Ocean by the penetration of the Kuroshio Current (KC), a strong western boundary warm current [Farris and

Wimbush, 1996]. Field observations suggested a general uplift of nutricline and thermocline in the NSCS in contrast to that in the KC, as the nutrient rich intermediate water flowing out of the NSCS through Luzon Strait to join the northward flowing Kuroshio mainstream [Tian *et al.*, 2006; Dai *et al.*, 2009], which originates from the low nutrient subtropical and tropical regions. The high nutrient intermediate water of the NSCS relative to the KC is formed by the effective mixing of the upwelled deep water and the surface water at the intermediate layers [Liu *et al.*, 2002]. It was reported that the surface water of the KC near the Luzon Strait showed substantially higher *Trichodesmium* abundance and rates of nitrogen fixation in the summer when compared to the water of the central NSCS [Chen *et al.*, 2008]. The low concentration of *Trichodesmium* in the NSCS was explained as the lack of iron-binding organic ligands in the region, a hypothesis that would lead to possible iron limitation of nitrogen-fixation in the dust rich regions [Wu *et al.*, 2003]. *Trichodesmium*, the most important N₂-fixing diazotroph in tropical and subtropical oceans, has thus been used as an indicator-species for water masses transport through the Luzon Strait and further into the NSCS [Chen, 2005; Chen *et al.*, 2008]. It was also well observed that zooplankton abundance and species richness were significantly higher in the central NSCS than in the KC [Hwang *et al.*, 2007]. The physical and biological processes driving the difference of the two marine ecosystems of the NSCS and the KC, however, are still poorly addressed. Therefore, it is desirable to investigate the temporal dynamics of low-trophic planktonic communities and compare their underlying driving factors for these two very contrast ecosystems.

Coupled physical and biological models have been applied to study the spatial and temporal variability of chlorophyll, carbon, and primary production in the NSCS [Liu *et al.*, 2002; Chai *et al.*, 2009, Gan *et al.*, 2010, Lu *et al.*, 2011]. Using a three-dimensional model of the Regional Ocean Model System (ROMS), Gan *et al.* [2010] explored the ecosystem responses to wind-driven upwelling and river plume over the continental shelf of the NSCS, both of which were found to increase nutrient fluxes to the shelf leading to phytoplankton blooms. A one-dimensional ROMS model with carbon cycle for simulating the temporal variation of surface pCO₂ in the NSCS [Lu *et al.*, 2011] suggested that the pCO₂ variation of seawater was largely controlled by high-frequency physical dynamics in this region. Though the spatial and temporal patterns of hydrographic and biogeochemical variables in the NSCS have been relatively well studied, mechanisms for long-term variability of marine ecosystem and biogeochemical cycles in the NSCS remain inadequately understood [Liu *et al.*, 2013].

In this paper, a one-dimensional biogeochemical model was constructed to simulate the long-term variability of lower-trophic planktonic ecosystem for two pelagic time-series stations with one in the central NSCS (116°E, 18°N, referred as station S) and the other in the upstream Kuroshio near the Luzon Strait (122.5°E, 21.5°N, referred to as station K). Both of the two stations are far from the continental shelf with a bottom depth of >3000 m (Figure 1) where upwelling/downwelling driven by wind stress curl is an important driver for ocean dynamics. The biogeochemical model was developed by modifying a nitrogen-based NPZD model [Fasham *et al.*, 1990; Gruber *et al.*, 2006] by adding phosphorus cycle and diazotroph nitrogen-fixation. The physical part of the model was based on modifying the one-dimensional ROMS model [Shchepetkin and McWilliams, 2005; Troupin *et al.*, 2010] with focuses on two important processes: the vertical turbulence mixing and the Ekman pumping induced by wind stress curl. Monthly averaged data from varying sources including the National Centers for Environmental Prediction (NCEP), the Global Precipitation Climatology Project (GPCP), and the National Climate Data Center (NCDC) were used as the forcing fields for the model. Initial conditions derived from the field data at the two stations were used to spin up the model. The 1-D biogeochemical model was then validated through several field observations in the NSCS and the KC. With this model, we examine the long-term patterns of physical dynamics, nutrient fluxes, and planktonic community in the NSCS and in the KC. We compare the responses of low-trophic planktonic ecosystems to physical forcing including turbulence mixing and the upwelling/downwelling in these two regions. Our main goal is to address the mechanisms responsible for the considerably lower diazotroph abundance and rate of nitrogen fixation observed in the northern South China Sea water than in the Kuroshio water.

2. Method and Materials

2.1. Field and Satellite Observations

Field studies near the station S in the NSCS (Figure 1), which was close to the site of SEATS [Wong *et al.*, 2007a], were carried out in November 2013 with Research Vessel Shiyun-1 by the South China Sea

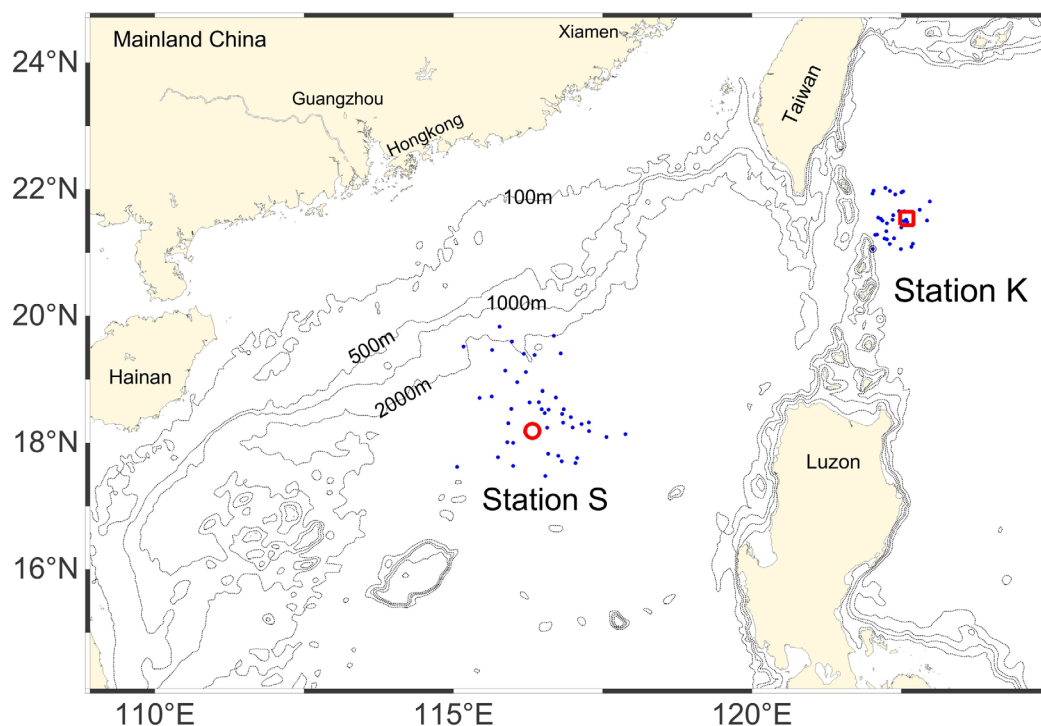


Figure 1. Location of the two study sites: station S (red circle) in the northern South China Sea and station K (red square) in the Kuroshio Current. Blue dots are positions of Argo observations near the two sites; lines represent the bathymetry of the South China Sea.

Institute of Oceanology. Hydrographic measurements were processed by Sea-Bird's 911 plus CTD. Discrete water samples were collected for biogeochemical measurements including chlorophyll and nutrients and measured using the standard methods [Li and Hansell, 2008]. Observations from the Array for Real-time Geostrophic Oceanography (ARGO) within the area of $115\sim 117.5^{\circ}\text{E}$, $17\sim 20^{\circ}\text{N}$ and the area of $121\sim 123^{\circ}\text{E}$, $21\sim 22^{\circ}\text{N}$ were used to generate the time series of temperature and salinity profiles for stations S and K, respectively. These data were acquired from the China ARGO Data Center (<http://www.argo.gov.cn>) (Figure 1). Data of Sea Surface Temperature (SST) and Sea Surface Chlorophyll-*a* (SSChl*a*) were acquired by satellite observations from NOAA's Environmental Research Division's Data Access Program (ERDDAP). Monthly averaged Sea Surface Temperature (SST) data from AVHRR were used to generate the time-series of temperature on the surface for the two stations. Ocean color records including weekly averaged Moderate Resolution Imaging Spectroradiometer (MODIS aqua) and Sea-viewing Wide Field-of-view Sensor (SeaWiFS) data were calibrated by field observations and used to create the time series of surface chlorophyll in the two study sites. For each station, two time-series of SSChl*a* from MODIS and SeaWiFS with different durations were merged into a longer time series from January 2000 to December 2013. For the data merged, the SeaWiFS data were adjusted by removing the systematic bias with respect to the MODIS data set according to a linear regression (similar to the approach of Liu *et al.* [2013]).

2.2. Model Configurations and Descriptions

Our simulations are based on coupling of a modified biogeochemical model with a one-dimensional version of ROMS, which is a primitive equations ocean model widely used by oceanographic modeling community [Shchepetkin and McWilliams, 2005; Gruber *et al.*, 2006; Chai *et al.*, 2009; Gan *et al.*, 2010; Troupin *et al.*, 2010]. The one-dimensional ROMS model includes a physical-biological coupling system, which defines a vertical coordinate system with increased resolution near the surface boundary layer [Troupin *et al.*, 2010], and an embedded mixed layer model with a vertical turbulence mixing closure of K-Profile Parameterization (KPP) [Large *et al.*, 1994]. Following the approach of Chifflet *et al.* [2001], we modify the one-dimensional ROMS model by including the process of vertical advection driven by wind stress curl, which is one of the most important processes responsible for the dynamics of the South China Sea [Metzger, 2003]. We modify

the nitrogen-based biological model [Fasham *et al.*, 1990; Gruber *et al.*, 2006] by adding processes of our interest including phosphorus cycle and nitrogen fixation, which have been suggested as important processes for primary production in the NSCS and KC [Wu *et al.*, 2003; Chen *et al.*, 2008]. The detail of model structures and configurations of the physical-biogeochemical coupling model will be described in the following sections.

2.2.1. Physical Model of Vertical Turbulence Mixing

The differential equations governing velocities (u and v), temperature (T), and salinity (S) are written as:

$$\frac{\partial u}{\partial t} = fv + \frac{\partial}{\partial z} \left(K_M \frac{\partial u}{\partial z} \right) - \frac{\partial}{\partial z} (wu) \quad (1)$$

$$\frac{\partial v}{\partial t} = -fu + \frac{\partial}{\partial z} \left(K_M \frac{\partial v}{\partial z} \right) - \frac{\partial}{\partial z} (wv) \quad (2)$$

$$\frac{\partial P}{\partial z} = -\rho g \quad (3)$$

$$\frac{\partial T}{\partial t} = \frac{\partial}{\partial z} \left(K_T \frac{\partial T}{\partial z} \right) - \frac{\partial}{\partial z} (wT) \quad (4)$$

$$\frac{\partial S}{\partial t} = \frac{\partial}{\partial z} \left(K_S \frac{\partial S}{\partial z} \right) - \frac{\partial}{\partial z} (wS), \quad (5)$$

where f is the Coriolis parameter; K_M , K_T , and K_S are the vertical turbulent mixing coefficient for momentum, temperature, and salinity, respectively; w is the vertical advection velocity. Density ρ is computed from pressure (P), salinity (S), and potential temperature (T) of the seawater using the equation of state of seawater. Vertical velocity (w) is assumed varying with depths. Here, we have made the depth (z) negative when going deep into the ocean.

At the sea surface, the model is driven by air-sea interactions including surface net heat flux, fresh water flux, and wind stresses. Surface boundary conditions for momentum, T and S ($w=0$ at the surface of $z=0$) are:

$$K_M \frac{\partial u}{\partial z} = \tau_{surf}^x \quad \text{and} \quad K_M \frac{\partial v}{\partial z} = \tau_{surf}^y \quad (6)$$

$$K_T \frac{\partial T}{\partial z} = \frac{Q_T}{\rho_0 C_p} \quad \text{and} \quad K_S \frac{\partial S}{\partial z} = \frac{(E-P)S}{\rho_0} \quad (7)$$

where, τ_{surf}^x and τ_{surf}^y are the surface wind stress components; $(E-P)$ is the evaporation minus the precipitation (Figure 2); Q_T is the net surface heat flux and C_p is the heat capacity. A bulk fluxes algorithm [Fairall *et al.*, 1996] was used to calculate each component of surface heat fluxes and freshwater fluxes from input data of cloud corrected short-wave and long-wave radiations, sea level air temperature, precipitation, relative humidity, surface wind vector. Surface wind stress was computed by $\tau = \rho_a C_d |W_{10}| W_{10}$, with W_{10} representing the vectors of wind velocity at 10m above the sea, ρ_a the density of air and C_d the dimensionless drag coefficient (calculated from its relationship with wind speed, Fairall *et al.* [1996]). Monthly data of short-wave and long-wave radiations, air temperature, and specific humidity are acquired from $2.5^\circ \times 2.5^\circ$ grid NCEP reanalysis. Monthly precipitation data are from GPCP that combines observations and satellite precipitation data into $2.5^\circ \times 2.5^\circ$ global grids. Data of monthly wind vector at 10 m are from NCDC with a resolution of $0.25^\circ \times 0.25^\circ$.

The vertical mixing processes in ROMS are parameterized by the KPP boundary layer scheme [Large *et al.*, 1994]. In the KPP model, two different scheme formulations are used for the surface boundary layer and the ocean interior, respectively. Within the boundary layer, the boundary layer similarity theory is applied to the water column, while the parameterization at the interior is focused on mixing effects associated with local shear, internal wave and double diffusion [Large *et al.*, 1994; Shchepetkin and McWilliams, 2005; Troupin *et al.*, 2010].

Several factors including the surface forcing, the buoyancy, and the velocity would influence the depth of the boundary layer, which is determined as the depth (d) when the bulk Richardson number Ri_b reaches its critical value Ri_{bc} . The value of Ri_b is expressed as:

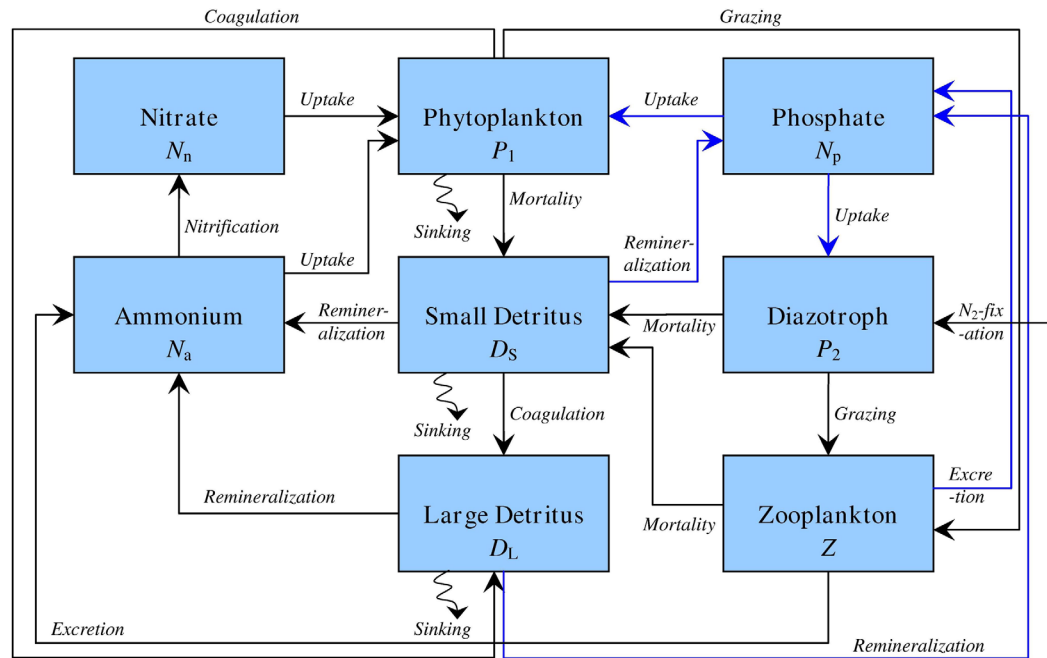


Figure 2. Diagram of biological model compartments with nitrogen and phosphorus flows in the system.

$$Ri_b = \frac{[B_r - B]d}{|V_r - V|^2 + V_t^2} \tag{8}$$

where B and V are the buoyancy and velocity with B_r and V_r representing the average buoyancy and velocity at the reference depth, respectively; V_t is an estimate of the turbulent contribution to velocity shear. In this study, a critical bulk Richardson number Ri_c of 0.3 was used. When buoyancy forcing is stable, the boundary layer depth is finally estimated by the minimum among the Monin-Obukhov length scale, the Ekman depth (d_e), and the value of d determined by equation (8).

2.2.2. Physical Model of Ekman Pumping by Wind Stress Curl

The one-dimensional physical model takes into account the effect of Ekman pumping driven by local wind stress curl. The Ekman pumping velocity (w_e) is expressed as [Gill, 1982]

$$w_e = \frac{1}{\rho_w} \left(\nabla \times \frac{\tau}{f} \right) \tag{9}$$

where, ρ_w is the density of seawater, which is assumed constant at 1024 kg m^{-3} ; f is the Coriolis parameter; τ is the monthly vector of wind stress around the time-series stations. The vertical velocity (w) is assumed varying with depths (z) as a sinusoid shape: $w = w_e \cdot \sin[(z/d_e) \times \pi/2]$, when $d_e \leq z \leq 0$ and $w = w_e \cdot \sin[(z-z_0)/(d_e - z_0) \times \pi/2]$, when $z_0 \leq z < d_e$. This relationship will guarantee a vertical velocity of zero at the surface and the bottom (z_0) of model domain, but a maximal vertical velocity (w_e) at the depth of Ekman layer (d_e).

Monthly $0.25^\circ \times 0.25^\circ$ grid wind data from National Climate Data Center (NCDC) from January 1994 to September 2011 was merged with the $1^\circ \times 1^\circ$ grid wind data of the Fleet Numerical Meteorology and Oceanography Center (FNMOC) from October 2011 to December 2013 to produce a continuous data set of wind vector from January 1994 to December 2013. These data are used for calculating wind stress and wind stress curl at the time-series stations and compared to results of $0.25^\circ \times 0.25^\circ$ grid wind data of QuikSCAT (QSCAT) (Figure 3), which was retired after October 2009. For both stations S and K, there were generally good agreements for the surface wind speeds (W_{10}) computed from NCDC, QSCAT, and FNMOC (Figures 3a and 3c). The relatively lower W_{10} of FNMOC during the summer compared to that of NCDC and QSCAT could be attributed to its lower spatial resolution. Though the Ekman pumping velocities (w_e) showed somewhat larger discrepancies among the three wind products, their general trends were again very similar

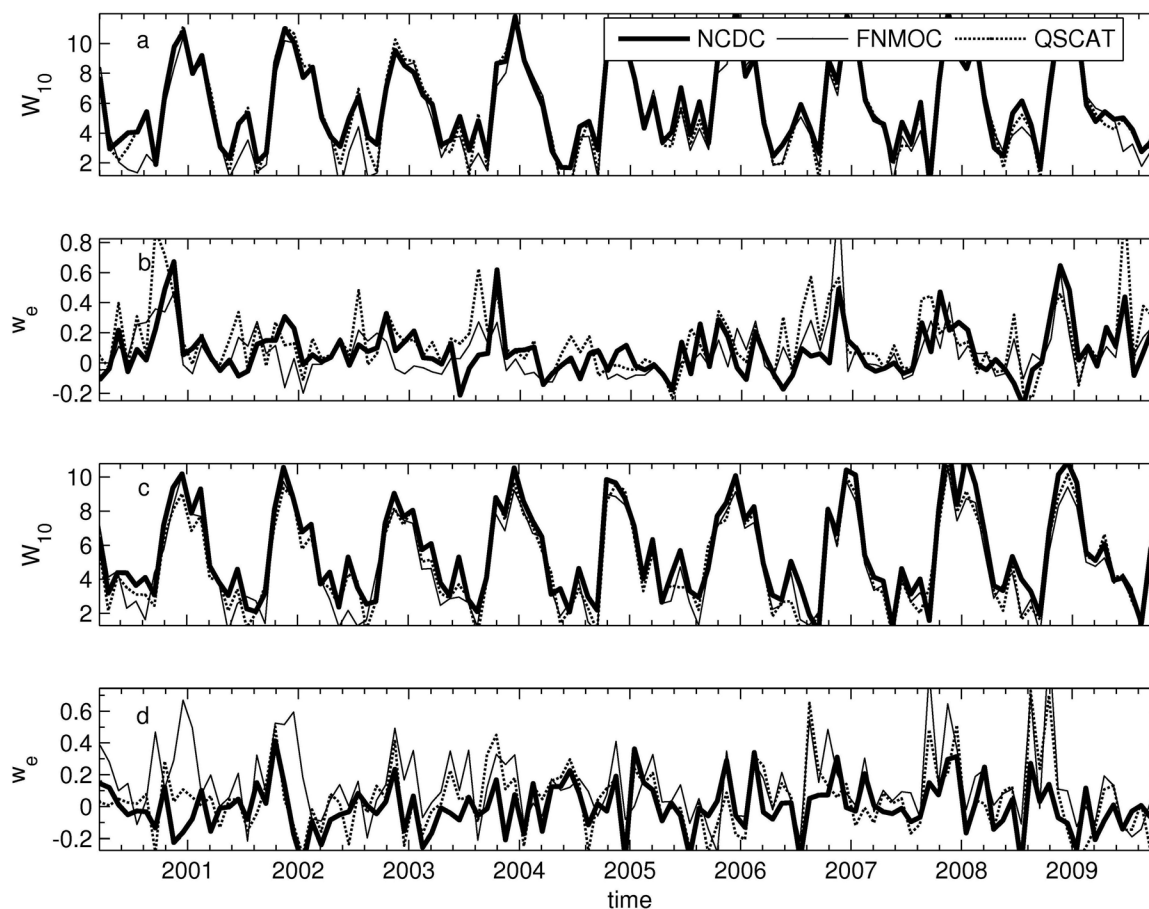


Figure 3. Comparisons of wind speeds (W_{10} , m/s) and Ekman velocities (w_e , 10^{-5} m/s) computed from different wind products including NCDC, FNMOC, and QSCAT in station S (a, b) and station K (c, d).

(Figures 3b and 3d). The NCDC data were chosen here for computing wind stress and wind stress curls because of its longer covering time and higher spatial resolution.

The actual vertical velocity in the ocean should be induced by a 3-D regional Ekman pumping process that is much complex than a local wind curl considered here. In order to account for the influences of horizontal processes on the 1-D model, the concentrations of tracers (T , S , and Nutrients) were relaxed toward their initial values with a nudging time determined by $t=4+16e^{z/100}$, which gives a value of t of about 6 years below 200 m and up to 20 years at the surface. The relaxation would allow the model to have a higher nutrient concentration in the deep water of the NSCS than that of the KC, which is driven by the regional deep circulations but is not taken into account by the model.

2.2.3. Biogeochemical Model

Our biogeochemical model modified from the nitrogen-based NPZD model [Fasham *et al.*, 1990; Gruber *et al.*, 2006] includes eight compartments: nitrate (N_n), ammonium (N_a), phosphate (N_p), phytoplankton (P_1), diazotroph (P_2), zooplankton (Z), small detritus (D_s), and large detritus (D_L) (Figure 2). All these compartments are connected through various rate processes. For nitrogen flow, fluxes within these compartments allow a functional difference between new production (fueled mainly by nitrate) and regenerated production (fueled by ammonium). Recent studies suggested that N_2 fixation by diazotrophs is an important source of new production in the NSCS [Wong *et al.*, 2007a, b; Chen *et al.*, 2008]. We therefore incorporated two different functional groups of phytoplankton in the model: one is diazotroph that is capable of fixing atmospheric N_2 and the other is nondiazotroph phytoplankton that is subject to nitrogen limitation when dissolved inorganic nitrogen is low. Here, we have assumed that diazotroph obtains nitrogen for growth only through N_2 fixation without uptake of inorganic nitrogen or organic nitrogen [Hood *et al.*, 2001; Fennel *et al.*, 2002]. The capability of diazotrophs using dinitrogen as the sole nitrogen source would result in an

increase of bioavailable nitrogen compared to phosphorus in the system. The new nitrogen source from N₂ fixation would drive the system from nitrogen-limitation to phosphorous-limitation in a long run, and influence ocean carbon cycle. Since the phytoplankton in the NSCS may also be well phosphorus limited near the continental shelf during the fall [Xu et al., 2008], we have added a full phosphorus cycle in the model and allow for phosphorus limitation of primary production in the system. Export production by vertical sinking of particles is also included in the model by assigning phytoplankton, small detritus, and large detritus different sinking velocities.

Photosynthetically available radiation (PAR), the total energy used for photosynthesis by phytoplankton, is derived from the attenuation of surface solar radiation with depths by seawater and phytoplankton, which should be properly parameterized [Gruber et al., 2006; Troupin et al., 2010; Li et al., 2010]. The PAR at sea surface is set as 43% of the shortwave solar radiation. Then, attenuation coefficient within each grid box is calculated based on the chlorophyll-*a* concentration inside the grid box, and the PAR is computed according to:

$$PAR_i = PAR_{i+1} \exp \{ -0.5(k_{water} + k_{chla}[Chla1_i + Chla2_i])\Delta z_i \} \tag{10}$$

where k_w and k_{chla} are the attenuation coefficients for water and chlorophyll; $Chla1$ and $Chla2$ are the chlorophyll concentrations of diazotroph and nondiazotroph phytoplankton, which are computed from their biomass and chlorophyll to carbon ratios (θ_i), assuming a constant C:N ratio of 6.625; Δz is the height of the vertical grid layer and i is the cell index, from 1 at the bottom to N at the top.

In the model, phytoplankton growth is limited by temperature T , light I (PAR), and nutrients including nitrate, ammonium, and phosphate. The growth rate of phytoplankton is written as

$$\mu_1(T, I, N_n, N_a, N_p) = \mu_1^{max}(T, I) \cdot \gamma(N_n, N_a, N_p) \tag{11}$$

where, μ_1^{max} is the nutrient-saturated maximal growth rate; $\gamma(N_n, N_a, N_p)$ is the nutrient-limitation expressed as $\gamma(N_n, N_a, N_p) = \min[\gamma(N_n, N_a), \gamma(N_p)]$ with $\gamma(N_n, N_a) = \gamma(N_n) + \gamma(N_a)$ and the half-saturated formula for $\gamma(N_n), \gamma(N_a), \gamma(N_p)$ given by

$$\gamma(N_n) = \frac{N_n}{(N_n + K_n)} \frac{K_a}{(N_a + K_a)}, \gamma(N_a) = \frac{N_a}{(N_a + K_a)} \text{ and } \gamma(N_p) = \frac{N_p}{(N_p + K_{p1})}$$

with K_n, K_a, K_{p1} representing the half-saturation constants for uptake of nitrate, ammonium, and phosphate. The N:P ratio for nondiazotroph (r_1) is assumed conform to the classical Redfield ratio of 16.

The nutrient-saturated maximal growth rate of phytoplankton as a function of light, temperature, and chlorophyll to carbon ratio is given by

$$\mu_1^{max}(T, I) = \frac{\mu_1^T(T) \alpha_1 I \theta_1}{\sqrt{(\mu_1^T(T))^2 + (\alpha_1 I \theta_1)^2}} \tag{12}$$

with $\mu_1^T(T) = 0.59 \cdot (1.066)^T$ according to Eppley [1972].

Growth rate of diazotroph is assumed only limited by temperature, light, and phosphate in the model and can be expressed as

$$\mu_2(T, I, N_p) = \mu_2^{max}(T, I) \cdot \chi(N_p) \tag{13}$$

where, μ_2^{max} is the nutrient-saturated maximal growth rate of diazotroph given by

$$\mu_2^{max}(T, I) = \frac{\mu_2^T(T) \alpha_2 I \theta_2}{\sqrt{(\mu_2^T(T))^2 + (\alpha_2 I \theta_2)^2}} \tag{14}$$

with $\mu_2^T(T) = 0.12 \cdot (1.066)^T$ based on the fact that diazotroph generally grows at a much lower rate than nondiazotroph phytoplankton [Hood et al., 2001; Fennel et al., 2002]. Effect of phosphate limitation of diazotroph growth is written as $\chi(N_p) = \frac{N_p}{(N_p + K_{p2})}$ with K_{p2} the half-saturation constant of phosphate uptake by diazotroph. We have assigned a much higher N:P ratio of 45 for diazotroph (r_2) compared to nondiazotroph phytoplankton according to Fennel et al. [2002].

In the model, the sources and sinks terms for the biomass variations of phytoplankton (P_1), diazotroph (P_2), and zooplankton (Z) are expressed as:

$$\frac{\partial P_1}{\partial t} = \mu_1^{\max}(T, I) \cdot \gamma(N_n, N_a, N_p) \cdot P_1 - g_Z Z \frac{P_1}{\lambda_p + P_1 + P_2} - \eta_p P_1 - k^c P_1 \cdot (P_1 + D_s) \quad (15)$$

$$\frac{\partial P_2}{\partial t} = \mu_2^{\max}(T, I) \cdot \chi(N_p) \cdot P_2 - g_Z Z \frac{P_2}{\lambda_p + P_1 + P_2} - \eta_p P_2 \quad (16)$$

$$\frac{\partial Z}{\partial t} = g_Z \beta_Z Z \cdot \frac{P_1 + P_2}{\lambda_p + P_1 + P_2} - \xi_Z Z - \eta_Z Z^2 \quad (17)$$

Fluxes of nitrate (N_n), ammonium (N_a), and phosphate (N_p) in the biogeochemical system are given by:

$$\frac{\partial N_n}{\partial t} = -\mu_1^{\max}(T, I) \cdot \gamma(N_n, N_a, N_p) \cdot \frac{\gamma(N_n)}{\gamma(N_n, N_a)} \cdot P_1 + k^{\text{nitrate}}(I) \cdot N_a \quad (18)$$

$$\frac{dN_a}{dt} = -\mu_1^{\max}(T, I) \cdot \gamma(N_n, N_a, N_p) \cdot \frac{\gamma(N_a)}{\gamma(N_n, N_a)} \cdot P_1 - k^{\text{nitrate}}(I) \cdot N_a + \xi_Z Z + k_5^r D_s + k_4^l D_L \quad (19)$$

$$\frac{\partial N_p}{\partial t} = -\mu_1^{\max}(T, I) \cdot \gamma(N_n, N_a, N_p) \cdot \frac{P_1}{r_1} - \mu_2^{\max}(T, I) \cdot \chi(N_p) \cdot \frac{P_2}{r_2} + \xi_Z \frac{Z}{r_1} + k_5^r \frac{D_s}{r_1} + k_4^l \frac{D_L}{r_1} \quad (20)$$

Governing equations for small (D_s) and large detritus (D_L) are given by:

$$\frac{\partial D_s}{\partial t} = g_Z (1 - \beta_Z) \cdot Z \cdot \frac{P_1 + P_2}{\lambda_p + P_1 + P_2} + \eta_p (P_1 + P_2) + \eta_Z Z^2 - k^c D_s (P_1 + D_s) - k_5^r D_s - \omega_s \frac{\partial D_s}{\partial z} \quad (21)$$

$$\frac{\partial D_L}{\partial t} = k^c (P_1 + D_s)^2 - k_4^l D_L - \omega_L \frac{\partial D_L}{\partial z} \quad (22)$$

The dynamic chlorophyll-*a* to carbon ratios for phytoplankton (θ_1) and diazotroph (θ_2) are expressed as (similar to Gruber *et al.* [2006]):

$$\frac{\partial \theta_1}{\partial t} = \mu_1^{\max}(T, I) \cdot \gamma(N_n, N_a, N_p) \cdot \left[\frac{\mu_1^T(T) \cdot \gamma(N_n, N_a, N_p) \cdot \theta_1^{\max}}{\sqrt{(\mu_1^T(T))^2 + (\alpha_1 \theta_1)^2}} - \theta_1 \right] \quad (23)$$

$$\frac{\partial \theta_2}{\partial t} = \mu_2^{\max}(T, I) \cdot \chi(N_p) \cdot \left[\frac{\mu_2^T(T) \cdot \chi(N_p) \cdot \theta_2^{\max}}{\sqrt{(\mu_2^T(T))^2 + (\alpha_2 \theta_2)^2}} - \theta_2 \right] \quad (24)$$

Parameters for the above equations (15–24) are shown in detail in Table 1. The values of these parameters are derived directly from literature [Fasham *et al.*, 1990; Gruber *et al.*, 2006; Troupin *et al.*, 2010; Li *et al.*, 2010] or from the field measurements in the NSCS.

2.2.4. Model Forcing and Initialization

The one-dimensional biogeochemical model was run for 20 years (from January 1994 to December 2013) with a time step of 600 s and a maximal depth of 400 m. The model followed a nonlinear coordinate of 100 layers with increased resolution in the surface. The model was forced by realistic air-sea fluxes, including net heat fluxes, fresh water fluxes, and surface wind stress (Figure 4), which has been described in the section 2.2.1. At the same time, the model was forced by local Ekman upwelling/downwelling driven by wind stress curl (section 2.2.2).

The model was initialized with temperature, salinity, nitrate, and phosphate acquired from the averaged field data of the stations during winter. The initial values for vertical mixing coefficients were taken to be 0.01 m²/s for momentum and 0.001 m²/s for temperature and salinity (similar to Troupin *et al.* [2010]). Vertical distributions of chlorophyll-*a* were taken from regression of mean profiles of the field data in winter. Initial profiles for other biogeochemical variables including ammonium, nitrogen biomass of phytoplankton and diazotroph, zooplankton, small and large detritus were estimated by the chlorophyll after multiplied by

Table 1. Values, Units, and Definitions for Parameters of the Biogeochemical Model^a

Parameter	Symbol	Value	Units
Half-sat. conc. for NO ₃ uptake (5)	K_n	0.8	mmol N m ⁻³
Half-sat. conc. for NH ₄ uptake (3,5)	K_a	0.1	mmol N m ⁻³
Half-sat. conc. for PO ₄ uptake by nondiazotroph	K_{p1}	0.05	mmol N m ⁻³
Half-sat. conc. for PO ₄ uptake by diazotroph	K_{p2}	0.03	mmol N m ⁻³
N:P ratio for nondiazotroph	r_1	16	mmol N : mmol P
N:P ratio for diazotroph (4)	r_2	45	mmol N : mmol P
Phytoplankton mortality to SDet rate (3)	η_p	0.07	day ⁻¹
Initial slope of P-I curve for nondiazotroph	α_1	7.0	mgC (mgChla Wm ⁻² d) ⁻¹
Initial slope of P-I curve for diazotroph	α_2	4.0	mgC (mgChla Wm ⁻² d) ⁻¹
Maximum chlorophyll to carbon ratio (5)	θ^{\max}	0.041	mg Chla (mg C) ⁻¹
Zoo maximum growth rate (1,4)	g_z	1.0	day ⁻¹
Zoo assimilation efficiency (1,2,4)	β_z	0.75	—
Zoo half-sat. constant for grazing (1,2)	K_p	1.0	mmol N m ⁻³
Zoo quadratic mortality to Detritus (2)	η_z	0.1	day ⁻¹ (mmol N m ⁻³) ⁻¹
Zoo specific excretion rate (1,3)	ξ_z	0.1	day ⁻¹
Nitrification rate (3)	k^{nitr}	0.1	day ⁻¹
Particle coagulation rate (2)	k^c	0.005	day ⁻¹ (mmol N m ⁻³) ⁻¹
Remineralization rate of D_5 (3)	k_5^r	0.1	day ⁻¹
Remineralization rate of D_L (3)	k_L^r	0.1	day ⁻¹
Sinking velocity of phytoplankton (2)	ω_p	0.5	m day ⁻¹
Sinking velocity of D_5	ω_5	0.5	m day ⁻¹
Sinking velocity of D_L (2)	ω_L	10	m day ⁻¹
Light attenuation coeff. for seawater (1,2)	k_{water}	0.04	m ⁻¹
Light attenuation coeff. for chlorophyll (2)	k_{chla}	0.025	(m ² mg Chla) ⁻¹

^aParameters of the biological model: (1) *Fasham et al.* [1990], (2) *Gruber et al.* [2006], (3) *Troupin et al.* [2010], (4) *Fennel et al.* [2002], and (5) *Li et al.* [2010].

light penetrations and thus the phytoplankton photosynthetic productions. The net short-wave radiations in station S were slightly higher than that in station K during the summer and the winter but about the same during other seasons (Figure 4c). Station S showed somewhat lower net long-wave radiations but higher air temperatures and specific humidity compared to those in station K (Figure 4d). In particular, the maximal difference between the two stations during winter could be as large as ~10 W/m² for long-wave radiations, ~2°C for air temperature, and ~2% for specific humidity. These differences would lead to a higher net heat flux to the ocean in the model for station S when combining short-wave and long-wave radiations with other surface fluxes such as latent and sensible heat fluxes. Precipitation rates, which determine the surface salinity, were higher in station S than in station K during summer, but about the same during the winter (Figure 4e).

Wind speed was generally higher during winter but lower in summer as influenced by the seasonal monsoons (Figure 4a). Though wind speed in station S was slightly higher than in station K during the summer, there was however no much difference found between them in the rest of the year. Ekman pumping velocity by wind stress curl was substantially different between the two stations with more upwelling events found in station S but downwelling events in station K. The curl-driven upwelling varied substantially in both stations with higher velocities during fall-winter but lower velocities during spring-summer (Figures 4a and 4b). It was also noticeable that the temporal variation of Ekman velocity in station K was much noisier than that in station S, possibly due to its complex physical interactions.

3.2. Variability of Sea Surface Temperature (SST) and Chlorophyll-a (SSChla) in the NSCS and the KC

The modeled SST in stations S and K were in reasonable agreement with the satellite observations with similar seasonal variability (Figure 5). Generally, the surface temperature in the NSCS was higher during summer (August–September) but lower during winter (February–March), as a result of seasonal monsoon forcing [*Liu et al.*, 2002]. The negative correlations between SST and wind speed in both stations (Figures 4 and 5) could be attributed to the wind-induced mixing and Ekman pumping that brought cold waters to the surface. Both model and satellite observation suggested that there was little difference of SST (Figures 5a and 5c) between the two stations possibly due to their similar shortwave radiations and wind speeds (Figures 4a and 4c). Surface salinity of the NSCS (data not shown) showed opposite seasonal trends compared to temperature, with low salinity of ~33.6‰ in around September but high salinity of ~34.1‰ in early April, which could be attributed to decrease of precipitation in winter leading to seasonal low freshwater fluxes at the

proper conversion factors. The model was spun up for the first 6 years to reach a steady status before our actual simulation from January 2000 to December 2013.

3. Results and Discussion

3.1. Seasonality of Surface Air-Sea Forcing and Ekman Pumping in the NSCS and the KC

Seasonal patterns of the surface forcing fields at the two study sites were generally similar (Figure 4). For both stations, there was an increase of short-wave radiation and a decrease of long-wave radiations during summer (Figure 4c), which should control the seasonal

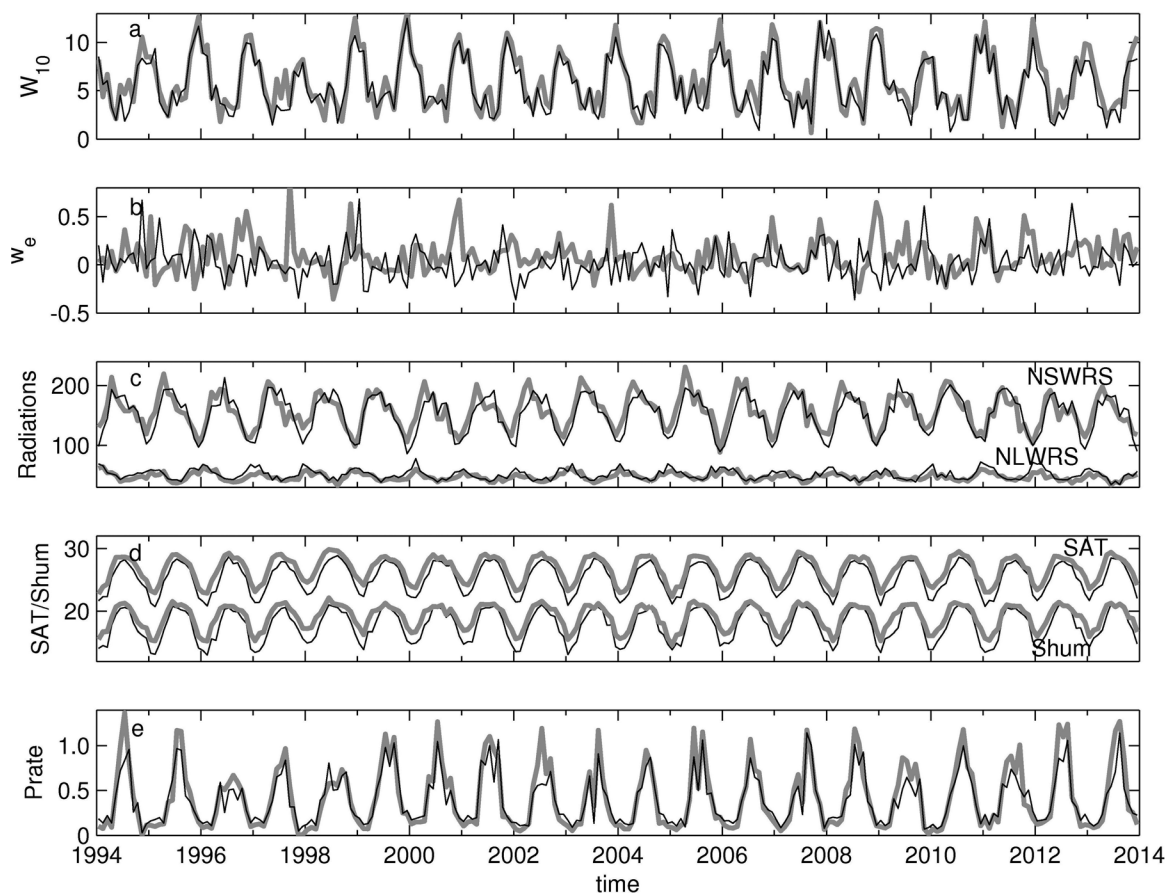


Figure 4. Comparisons of monthly mean forcing sequences including (a) wind speed at 10 m height (W_{10} , m/s), (b) Ekman velocity (w_e , 10^{-5} m/s), (c) net short-wave and long-wave radiations (NSWRS and NLWRS, w/m^2), (d) sea-level air temperature (SAT, °C) and specific humidity ($Shum$, %), and (e) precipitation rate ($Prate$, cm/d) between the station S (gray) and the station K (black) from January 1994 to December 2013.

surface ocean. The model apparently underestimated SST during the summer of 2002 and 2013 in station S (Figure 5a) and the summer of 2013 in station K (Figure 5c). Nevertheless, the 1-D model captures a more regional signal, whereas the satellite observation may include small-scale spatial heterogeneity that is not resolved by the model.

Data of satellite ocean color had been questionable for its application near the shore of the NSCS [Shang *et al.*, 2014], but it was found valuable for studying the long-term climate impacts in the offshore regions of the central NSCS [Liu *et al.*, 2013]. The modeled SSChla showed a reasonable agreement with the satellite observations from ocean color (Figures 5b and 5d). Our results suggested a substantial interseasonal variability of SSChla for both the NSCS and the KC with a concentration difference up to 10 folds. The concentration of SSChla was generally high during the winter but low during the summer in the two sties. The seasonal variations of SSChla agreed well with the trends of wind speed in both stations, with a higher wind speed corresponding to a higher chlorophyll, suggesting that wind-induced vertical mixing and Ekman pumping in the surface ocean could have increased the fluxes of nutrient from the subsurface in these regions [Liu *et al.*, 2002]. Generally, the concentration of surface chlorophyll in station S is about twice of that in station K (Figures 5b and 5d), which may be due to the higher nutrient fluxes from the subsurface in the NSCS as the water temperature and light intensity were mostly the same for the two stations. The model, however, showed higher SSChla than observations during the winter of 2010–2011 in station S (Figure 5b) and the winter of 2010–2013 in station K (Figure 5d). The discrepancies could be caused by the increase of cloud coverage during these periods (data not shown), which resulted in large areas of missing satellite data in the study regions leading to underestimation of sea surface chlorophyll by satellite observation.

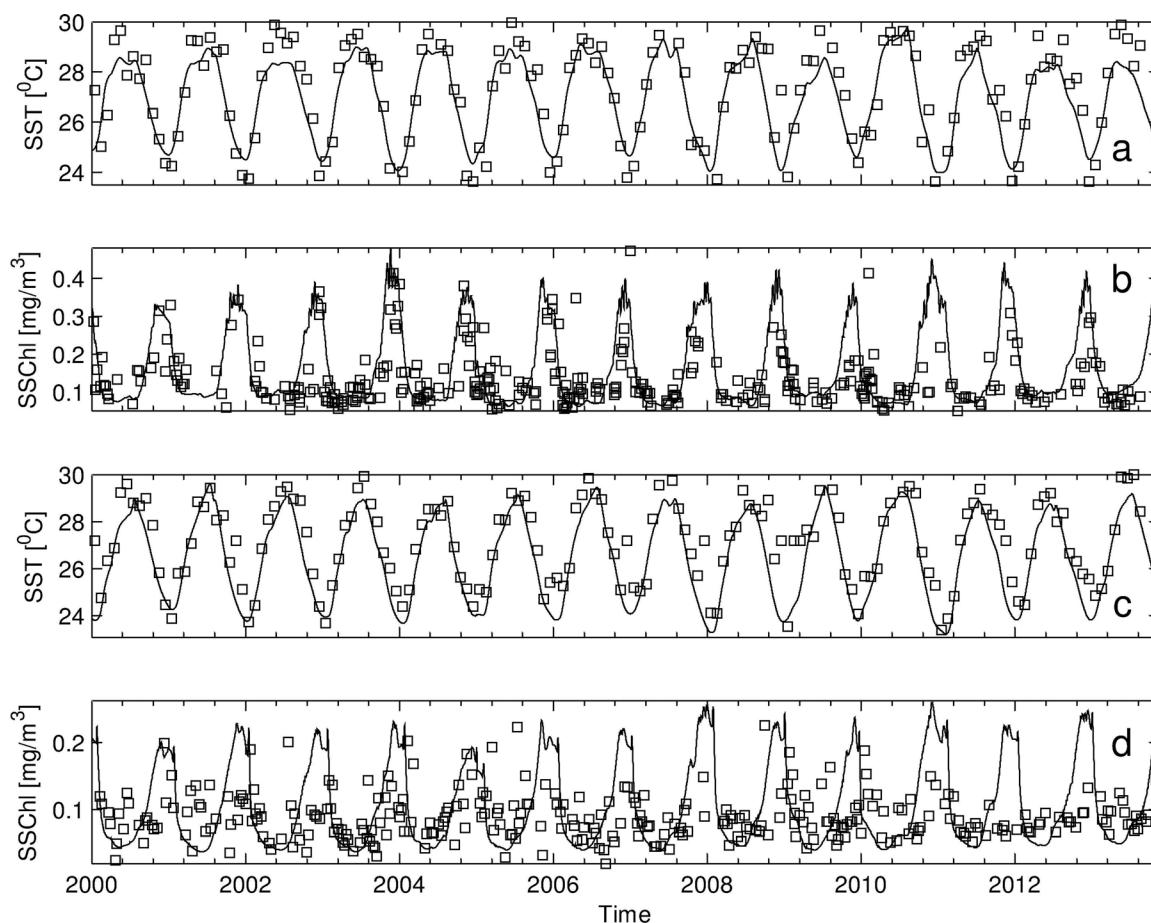


Figure 5. Comparison of sea surface temperature (SST) and sea surface chlorophyll-*a* (SSChl) between model predictions (lines) and satellite observations (boxes) for station S (a, b) and station K (c, d) from January 2000 to December 2013. SSChl are merged weekly data of SeaWiFS and MODIS-Aqua; SST are monthly data of AVHRR Pathfinder.

To assess the skill of model prediction, a Taylor diagram [Taylor, 2000] was constructed to statistically summarize how closely the model results matched observations in terms of the correlation, the centered root mean square difference and the standard deviations (Figure 6). Several data sets were used for the assessments, including satellite SST and SSChl from 2000 to 2013 and ARGO seawater temperature and salinity of 50m depth from 2005 to 2012. Model results from the hindcast simulation were generally well reproduce the observations with the correlation coefficient (r) ranged from 0.5 to 0.99, and the normalized standard deviation (NSD) from 0.5 to 1.2 (normalized by the standard deviation of the corresponding observed field, Taylor [2000]). The model exhibited promising skills in producing temporal variability of SST in station K, with the correlation coefficient greater than 0.95 and the NSD close to 1. Although the model simulation overestimated SSChl during the winter of some years (Figure 5), the model-data comparison of SSChl yielded a correlation coefficient of 0.55–0.75 and a NSD of 1.1–1.2. Overall, the model showed better skills in simulating the temporal variations of temperature at 50 m depth ($r=0.8-0.85$, $NSD=0.7-0.8$) than salinity ($r=0.5-0.6$, $NSD=0.5$) for both stations S and K, which could be due to underestimate of surface freshwater fluxes by the low spatial resolution of precipitation rates used in the model.

3.3. Temporal Evolution of Hydrography and Nutrient Biogeochemistry in the NSCS and the KC

The predicted monthly changes of the vertical temperature, salinity, and density by our model showed a reasonable agreement with the observations from ARGO in both the station S (Figure 7) and station K (Figure 8). A seasonal thermocline was generally formed during March–April in the NSCS due to the solar heating (Figures 4c and 5a), with the deepening of thermocline starting in August–September when the surface net heat fluxes became negative. The thermocline of the NSCS was much shallower than that of the KC as a result of its shallower mixed layer. The highest temperature and lowest salinity were often found during the

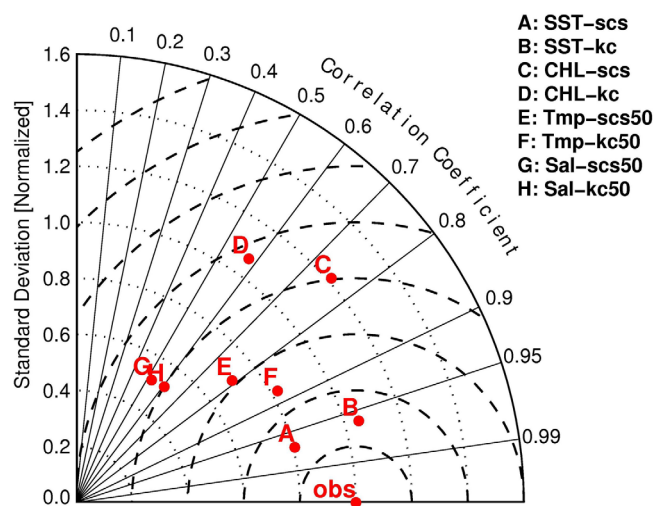


Figure 6. Taylor diagram for model skill assessments. Observations (obs) of stations S and K include sea surface temperature (A,B), sea surface chlorophyll (C,D), and ARGO temperature (E,F) and salinity (G,H) at 50 m depth.

early summer for both stations. Seawater temperature decreased with depths and reached about 15°C and 20°C at 200m in station S (Figure 7d) and station K (Figure 8d), respectively. The trends for salinity and density were opposite to that of temperature. Consistent with the observations, our model suggested a layer of salinity maximum around the depth of 200 m for both stations S and K (Figures 7e and 8e). Salinity in station K was slightly higher than that in station S possibly due to its lower precipitation rates (Figure 4). The modeled temporal fluctuations of hydrography in the subsurface of the station K were relatively smaller than the ARGO observations (Figure 8). For example, the sharp deepening of the 25° isotherm to 150 m depth from

December 2008 to January 2009 was not fully captured by the model, which suggested that other processes that were not considered in the 1-D model, such as the episodic vertical mixing induced by mesoscale eddies [McGillicuddy *et al.*, 2007], might also play an important role on the physical dynamics of the station. The influence of horizontal variability of Kuroshio on our model results of station K should be relatively small due to the low along-stream biogeochemical gradient. In addition, the current variability along Kuroshio in the study region should be reflected in the vertical motion due to continuity in our 1-D model. Interestingly, both observation and model suggested a substantially freshening of seawater salinity in the upper water column in station K from January 2009 to May 2009. In particular, the salinity isobar of 34.7‰ reached a depth of about 120 m in the spring of 2009 but generally outcrop to the surface for the same periods in both 2008 and 2010 (Figure 8e). The salinity anomaly we found could not be explained by change of precipitation, as the precipitation rate was even lower than that of the previous year (Figure 4e). Our model suggested that the salinity anomaly was induced by downwelling driven by negative wind stress curl from the late 2008 to the early 2009 (Figure 4b), which pushed the surface water with relatively low salinity down to more than 100 m depth and resulted in low salinity within the mixed layer. The finding of salinity anomaly in the upstream Kuroshio Current during the spring of 2009 could well explain the presence of a moderate El Niño event 6 months later. It was suggested that a barrier layer formed by salinity stratification, which separated the subsurface cold water from the surface mixed layer, was important for maintaining the heat buildup in the western Pacific Ocean, a necessary precursor for El Niño development [Maes *et al.*, 2005].

The modeled temporal patterns of nitrate and phosphate in the NSCS showed good agreements with observations at the station S from September 1999 to October 2003 (Figures 9a–9d). In particular, both model and observation suggested that the nutricline of station S was clearly pushed down in January 2000 but uplifted in October 2000, as a result of downwelling in January and upwelling in October induced by wind stress curls (Figure 4b). The relatively weaker of nutricline deepening in model than in observation during January 2000 could be caused by underestimate of the vertical velocity below the Ekman depth. There were strong seasonal cycles for all the nutrients in the subsurface layers (>150m) of both stations S and K (Figures 10a and 10b and Figures 11a and 11b) with the lowest nutrients during the summer but the highest nutrients during the winter, as a result of the strong convective mixing caused by northeast monsoons. A subsurface maximum of ammonium was always noticeable with a much higher concentration in the NSCS than in the KC (Figures 10c and 11c). Concentrations of nitrate and phosphate below the euphotic zone of the NSCS were significantly higher than that of the KC with difference up to six folds at the depth of 200 m (Figures 12a and 12e), which was a consequence of the model setup building on much higher nutrient concentrations observed in the deep water of the NSCS. The modeled surface nutrient concentrations were generally very low in both stations with the highest concentrations of ~0.2 μM nitrate, ~0.02 μM phosphate, and ~0.05 μM ammonium found in the winter (Figures 10 and 11), which agreed well with the

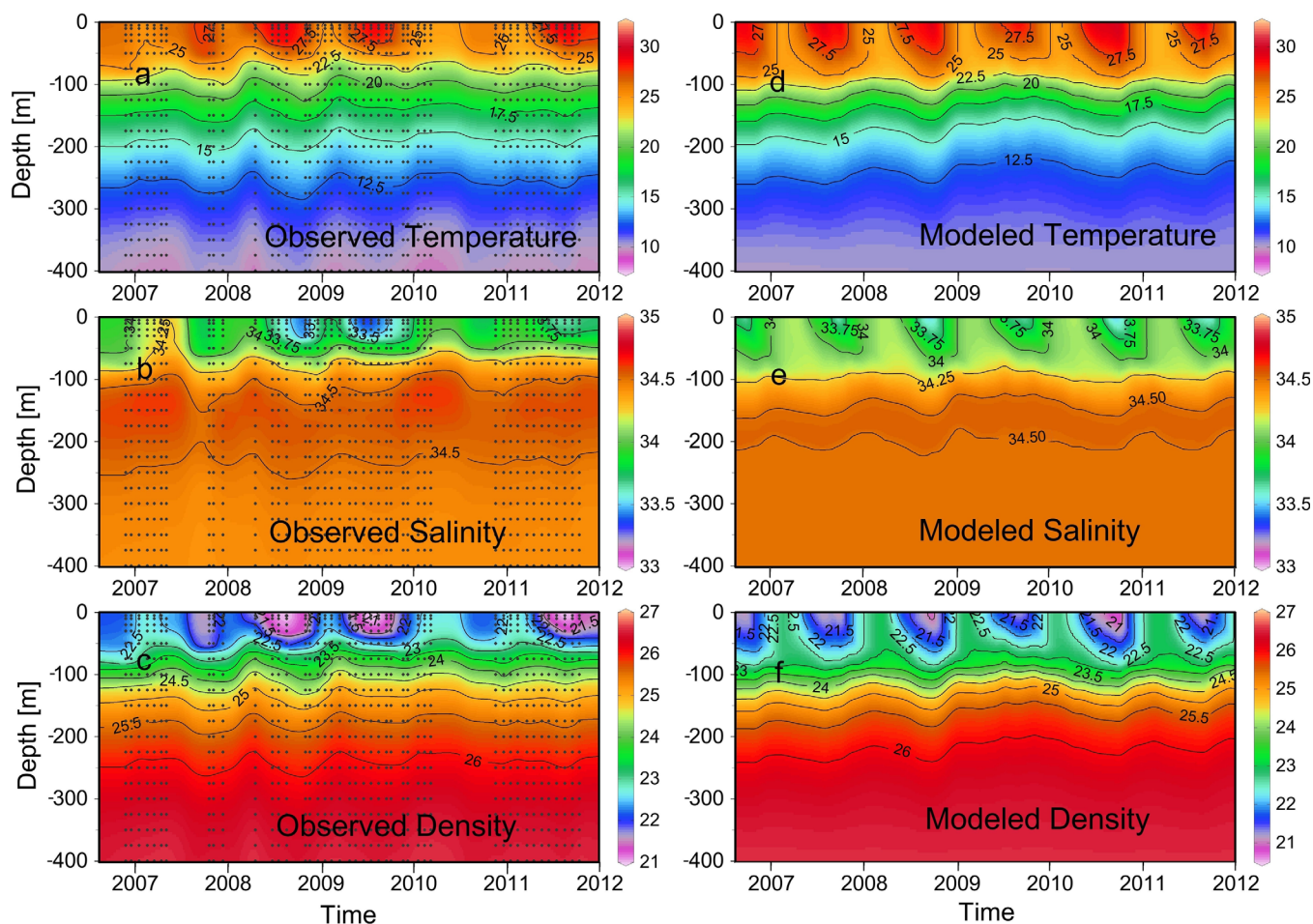


Figure 7. Comparisons of vertical distribution of temperature (a, d), salinity (b, e), and density (c, f) between Argo observations and model predictions for station S from 2006 to 2012.

low-level nutrient measurements in the regions [Wu *et al.*, 2003; Chen *et al.*, 2008]. Nutrient distributions within the euphotic zone, however, were significantly different between these two stations. Station K was subjected to the influence by a strong wind-induced deep mixing and Ekman pumping during the winter, which pushed the nutricline down to about 120 m depth leading to a substantially low nutrient condition in the bottom part of the euphotic zone. While, the subsurface nutricline in station S was generally uplifted during the winter (Figure 10a) and resulted in higher nutrient concentrations for phytoplankton production as a result of enhanced curl-driven upwelling (Figure 4a).

3.4. Temporal Variations of the Low-Trophic Planktonic Ecosystem in the NSCS and the KC

The modeled chlorophyll-*a* generally showed a subsurface maximum in both stations S and K during the most of the year, except in the winter when strong convective mixing led to a homogenous chlorophyll concentration within the euphotic zone. The subsurface chlorophyll maximum in the NSCS was relatively higher in the spring with a concentration up to 0.6–0.9 mg/m³, which often decreased to ~0.4 mg/m³ in the fall due to a combined effect of varying temperature, light and nutrients in the water column. The biomass of phytoplankton showed slightly different vertical distributions from chlorophyll, with subsurface biomass maximum located much shallower than the deep chlorophyll maximum (Figures 11d and 13a), which were common features of pelagic ecosystems as phytoplankton acclimated to the reduced light and increased nutrients in the water column by changing chlorophyll to carbon ratios [Li *et al.*, 2010]. The vertical patterns of modeled chlorophyll-*a* showed reasonable agreements with observations for both stations (Figures 12b and 12f), though the intense subsurface chlorophyll maxima in station S during the spring and the summer were not obvious in the field data (Figure 12b). The discrepancies of chlorophyll maxima

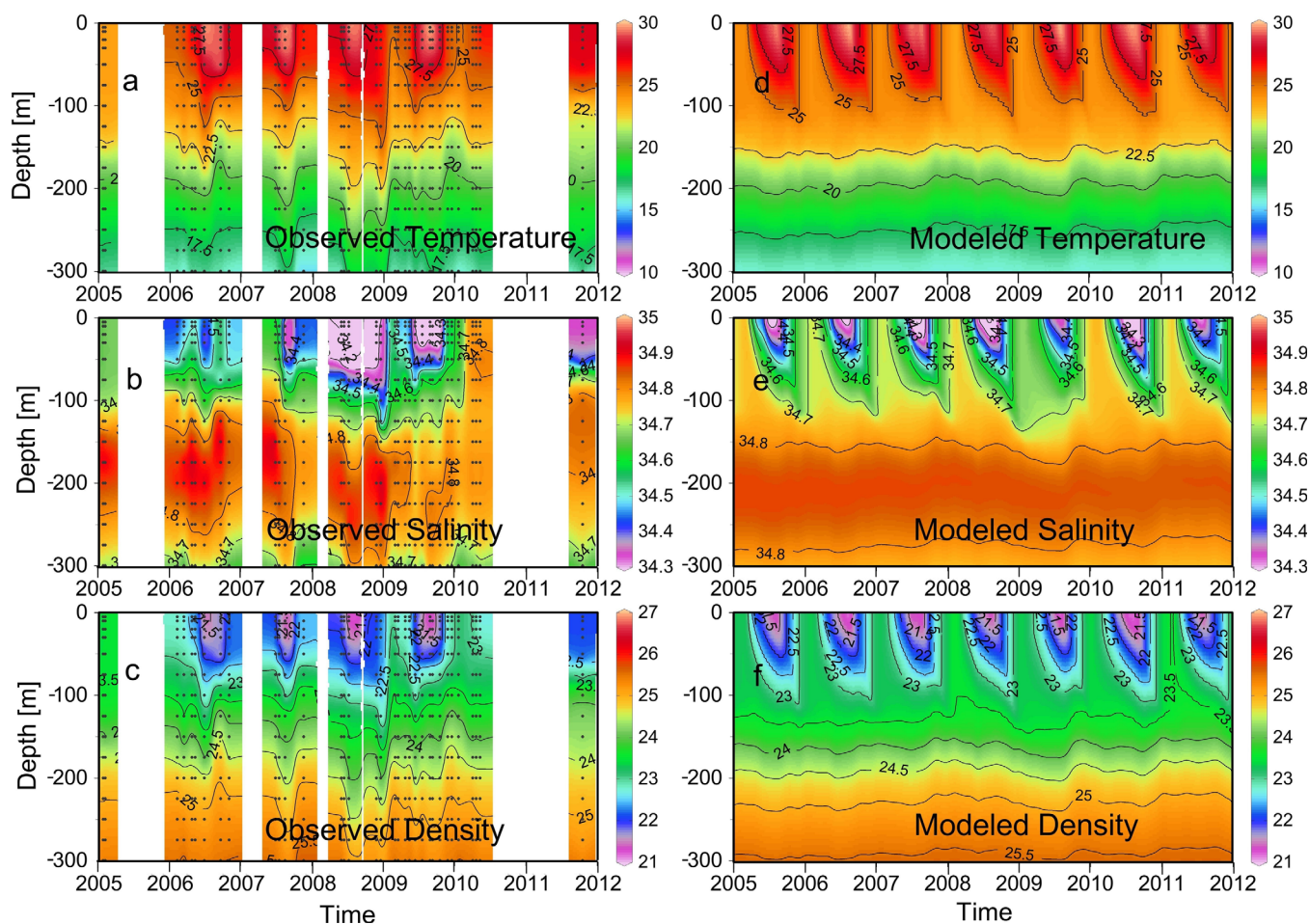


Figure 8. Comparisons of vertical distribution of temperature (a, d), salinity (b, e), and density (c, f) between Argo observations and model predictions for station K from 2005 to 2012.

between model and observation in the NSCS could be due to the inadequate field data (one profile only for each season).

Diazotroph was generally negligible all the year around in station S, but was found with high abundance during the summer in station K, which was consistent with previous field observations [Chen *et al.*, 2008]. N_2 -fixation by diazotrophs was also extremely high in station K during the summer compared to the rest of the year (Figure 13b) suggesting a stronger nitrogen limitation in the summertime (Figure 13e). High rate of N_2 fixation, up to $\sim 0.8 \text{ mgC/m}^3/\text{d}$ in the surface, was only found in station K but not in station S, which was also in good agreement with the field measurements (Figures 12d and 12h). Both diazotroph biomass and N_2 -fixation generally decreased with depths before reaching a value of zero above the nutricline as a result of strong light limitation for diazotrophs. The depth-integrated N_2 -fixation from model generally agreed well with observations in station K (Table 2). The model, however, did not capture the summer N_2 -fixation rate of $13 \mu\text{mol N m}^2 \text{ d}^{-1}$ in station S as the modeled rates was lower than the detection limit of observation. Nitrate-uptake-based new production was generally underestimated by the model in station K but was well consistent with observations in station S. Vertical integrations of primary production showed a reasonable agreement with observations for all the seasons in both stations S and K (Table 2).

The temporal variation of surface primary production generally followed the same tendency as the sea surface chlorophyll-*a* in both stations with the highest value found in the winter. Surface primary production during the winter in station K was relatively low ($\sim 14.4 \text{ mgC/m}^3/\text{d}$) and only about half of that in station S ($\sim 28.5 \text{ mgC/m}^3/\text{d}$). The predicted vertical distributions of primary production during the winter from the model agreed well with the observations for both stations, which decayed quickly with depths when approaching the nutricline (Figures 12c and 12g). Interestingly, the modeled primary production of station

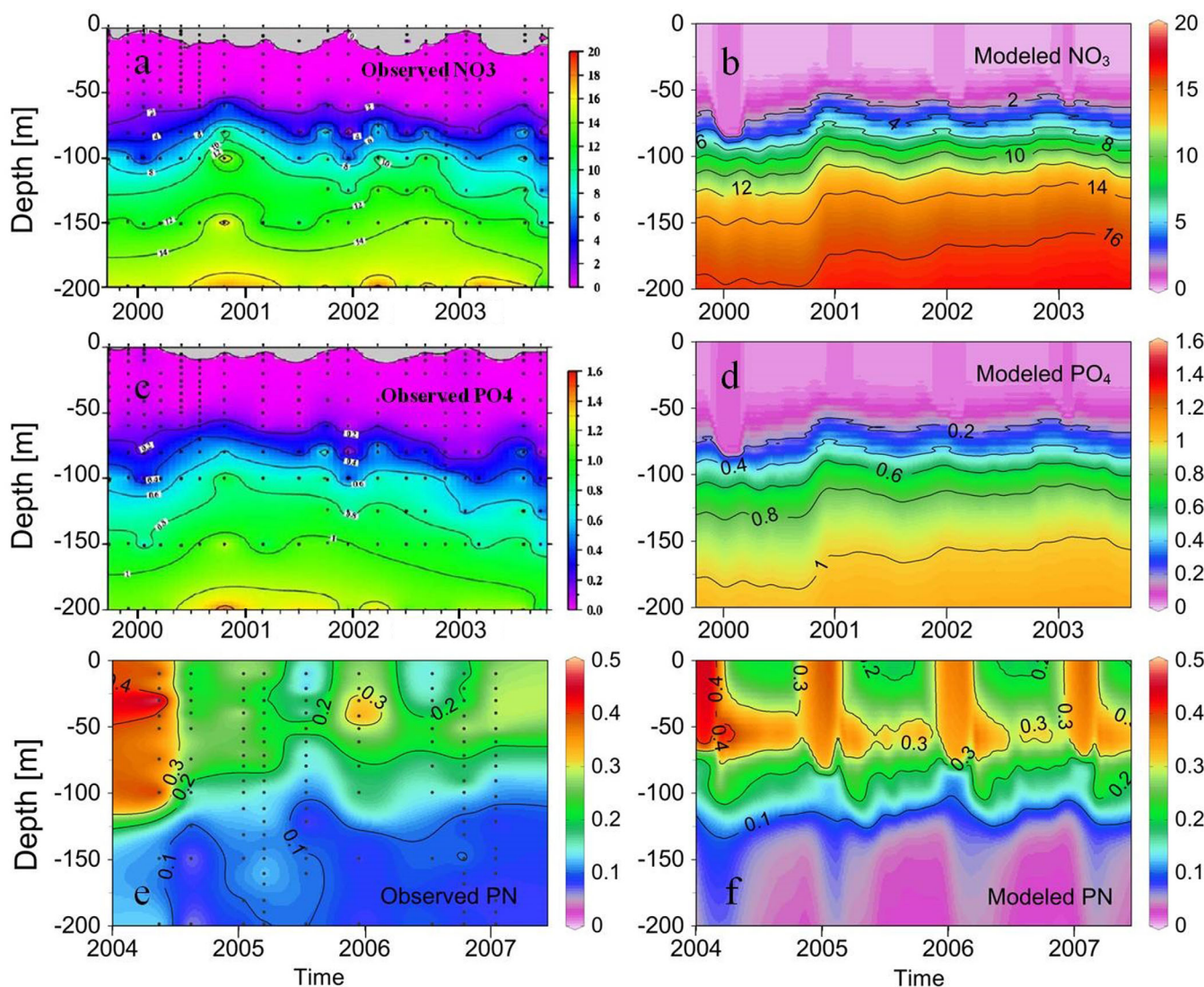


Figure 9. Comparisons of the vertical distributions of nitrate (NO_3), phosphate (PO_4), and particulate nitrogen (PN) between the observed (a, c, e) and the modeled results (b, d, f) for station S. NO_3 (a) and PO_4 (c) of September 1999 to October 2003 were reproduced from Wong *et al.* [2007a, 2007b] and PN (e) of May 2004 to January 2007 was from Kao *et al.* [2012]; unit is $\mu\text{mol/kg}$.

S during the spring and the summer showed double peaks with one on the surface and the other at the depth of the deep chlorophyll maximum (Figure 12c), which was not observed in some studies [Chen *et al.*, 2008] but had been frequently found in the large area of the central NSCS [Song *et al.*, 2010]. The second peak of primary production was contributed by the subsurface chlorophyll maximum, which was much weaker in the KC as a result of its lower nutrient concentration and deeper nutricline. The seasonal pattern of zooplankton generally followed that of phytoplankton as the result of direct predator-prey interaction, which led to a close correlation of biomass between the modeled zooplankton and phytoplankton ($Z = 2.016 P_1 - 0.0561$, $r^2 = 0.897$, $p < 0.01$). Consistent with our model results, field survey by towing the upper 200 m near the station S during 1997–1999 confirmed that zooplankton biomass was substantially higher in the winter than in the other seasons [Li *et al.*, 2004]. This was because both zooplankton community and assemblage would vary substantially during the monsoon transition period as an effect of monsoon forcing [Hwang *et al.*, 2007].

In the model, small detritus, usually including the fractions of dead organisms and the fecal materials, were derived from the decomposition of phytoplankton and zooplankton. Therefore, the seasonal variations of small detritus showed a similar trend as the phytoplankton (data not shown). Large detritus, however, showed substantially different vertical patterns from both phytoplankton and zooplankton with maximal

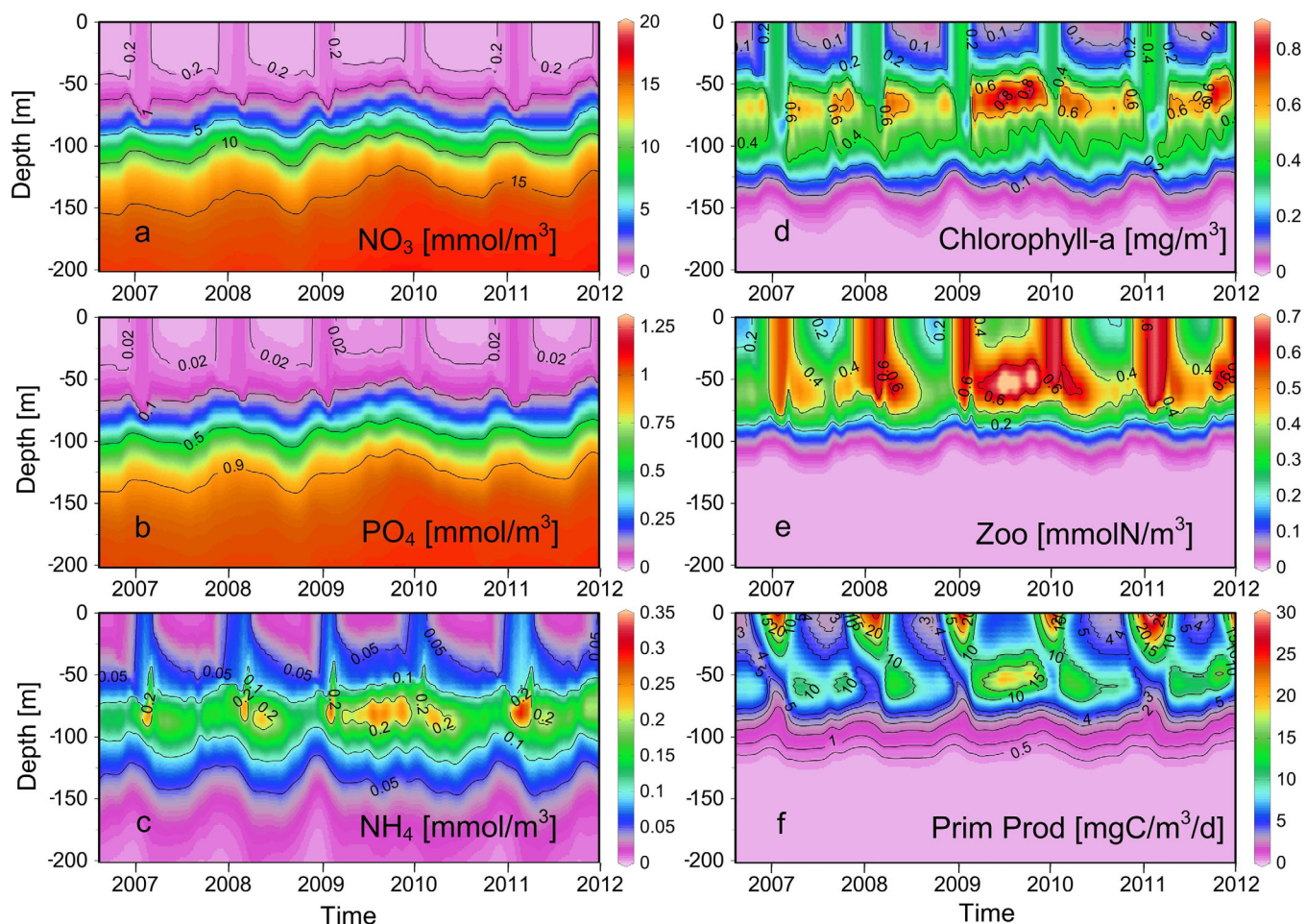


Figure 10. Time-series distributions of modeled nitrate (a), phosphate (b), ammonium (c), chlorophyll-a (d), zooplankton (e), and primary production (f) for station S from 2006 to 2012.

concentrations presented at depths below the euphotic zone, as the high sinking velocities often allow them escaping from the rapid recycling within the euphotic zone. The measured particulate nitrogen in station S from 2004 to 2007, which excluded the small detritus and zooplankton on purpose by selective filtrations [Kao *et al.*, 2012], showed a good agreement with our modeled particulate nitrogen estimated by combining nitrogen biomasses of phytoplankton and large detritus (Figures 9e–9f). In particular, both model and observation suggested that particulate nitrogen was very low below 100 m ($<0.2 \mu\text{M}$) with a clear subsurface maximum during the summer but a well-mixed euphotic zone of high particle concentrations during the winter.

3.5. The Impact of Physical Dynamics on Nutrient Fluxes, New Production, Community Structure in the NSCS and KC

When horizontal processes are ignorable, the vertical pattern of phytoplankton in the offshore regions should be determined by the balanced between the net growth of phytoplankton and the local transport of phytoplankton by turbulent diffusion [Troupin *et al.*, 2010; Li *et al.*, 2012]. Along with the diapycnal diffusion, vertical advection by episodic upwelling or downwelling could also influence the vertical gradients of phytoplankton and nutrients [Chifflet *et al.*, 2001]. In the upper layer of the open ocean such as the central NSCS and the upstream Kuroshio, horizontal fluxes of nutrients could be considered negligible due to their low horizontal gradients within the euphotic zone. The total contributions of physical transports to nitrate fluxes, including diffusion $J_{dif} = -K_s dN/dz$ and advection $J_{adv} = wN$ [Ledwell *et al.*, 2008], therefore could be expressed as

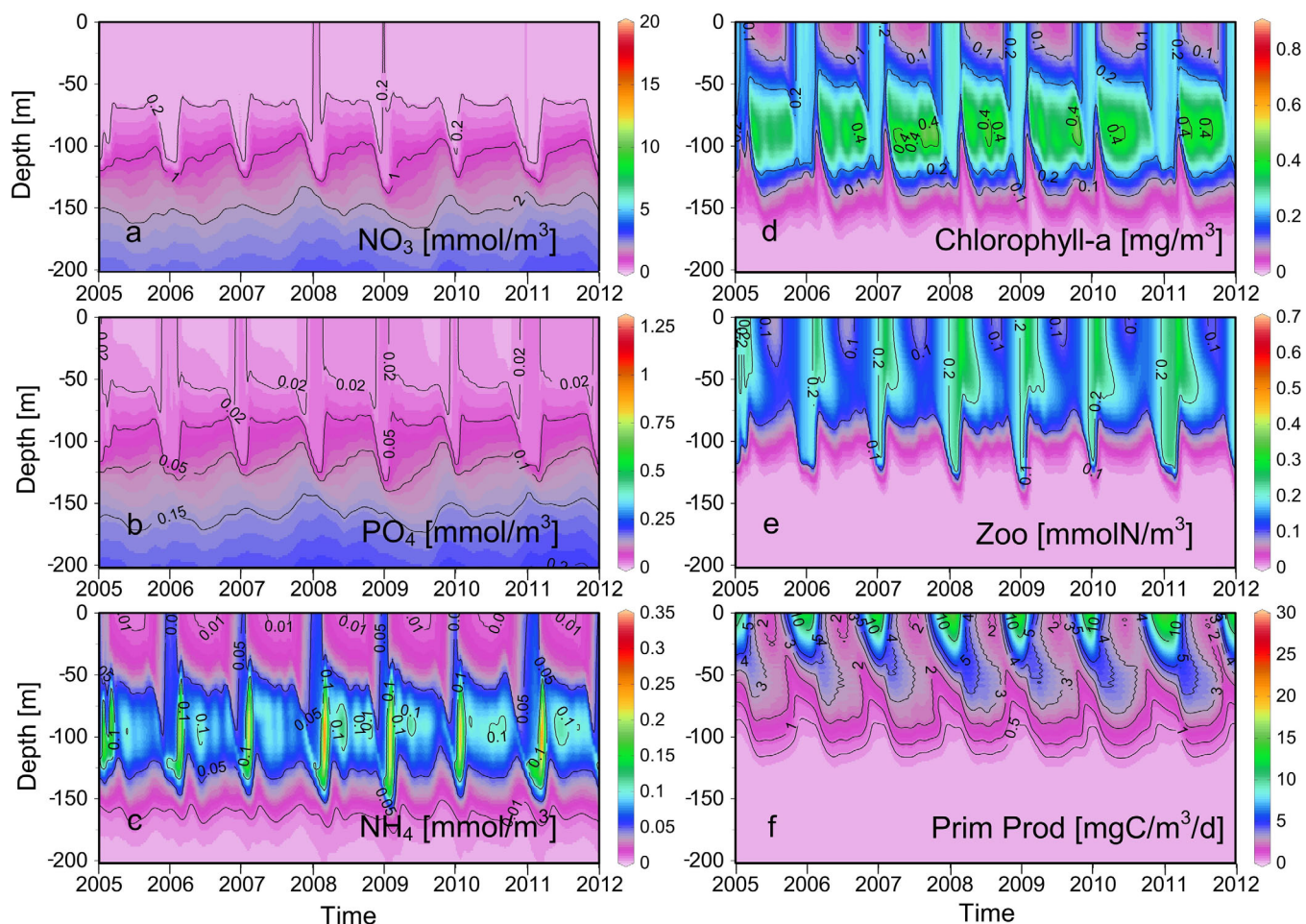


Figure 11. Time-series distributions of modeled nitrate (a), phosphate (b), ammonium (c), chlorophyll-a (d), zooplankton (e), and primary production (f) for station K from 2005 to 2012.

$$J_{total} = J_{dif} + J_{adv} = -K_s \frac{dN}{dz} + wN \quad (25)$$

There was large difference in the vertical gradients of nitrate between the two time-series stations with a substantially higher value in the NSCS (Figures 14b and 14f), as a result of its high nutrient intermediate waters. The position of deep chlorophyll maximum in the model generally followed the depth of maximal nitrate gradient or nitracline throughout the year for both stations S and K. The gradient of <0.02 mmolN/m⁴ during the summer in the upstream KC near the Luzon Strait was resemble to the condition of the oligotrophic subtropical gyres [Li and Hansell, 2008], where N₂ fixation contributed a large percentage to the new production [Hood et al., 2001; Fennel et al., 2002; Church et al., 2009]. Our results suggested that physical transport of nutrients above the nitracline was largely controlled by vertical turbulent mixing (Figures 14c and 14g), while vertical advection by sporadic upwelling and downwelling was important for nutrient transports below the nitracline (Figures 14d and 14h), which would determine the vertical oscillations of isopycnal surface and the depth of nutricline.

The large discrepancy of diffusive nitrate fluxes between stations S and K was mainly due to the large difference of nitrate gradients between the two stations (Figure 15a), as the profiles of their vertical mixing coefficients were quite similar (Figure 15a). Our model revealed that the seasonal patterns of diffusive nitrate fluxes were substantially different between the two stations. High diffusive nitrate fluxes of >1.2 mmolN/m²/d over a shallow nutricline during the winter of both stations (Figures 14c and 14g) were consistent with the enhanced vertical mixing by winter convective overturn, which was reinforced by wind-induced mixing [Tseng et al., 2005]. The seasonal variations of nutrient fluxes would have driven the ecosystem fluctuations by a way of bottom-up control mechanism. For example, the abnormally high fluxes of nitrate (~ 2.4 mmolN/m²/d) at the

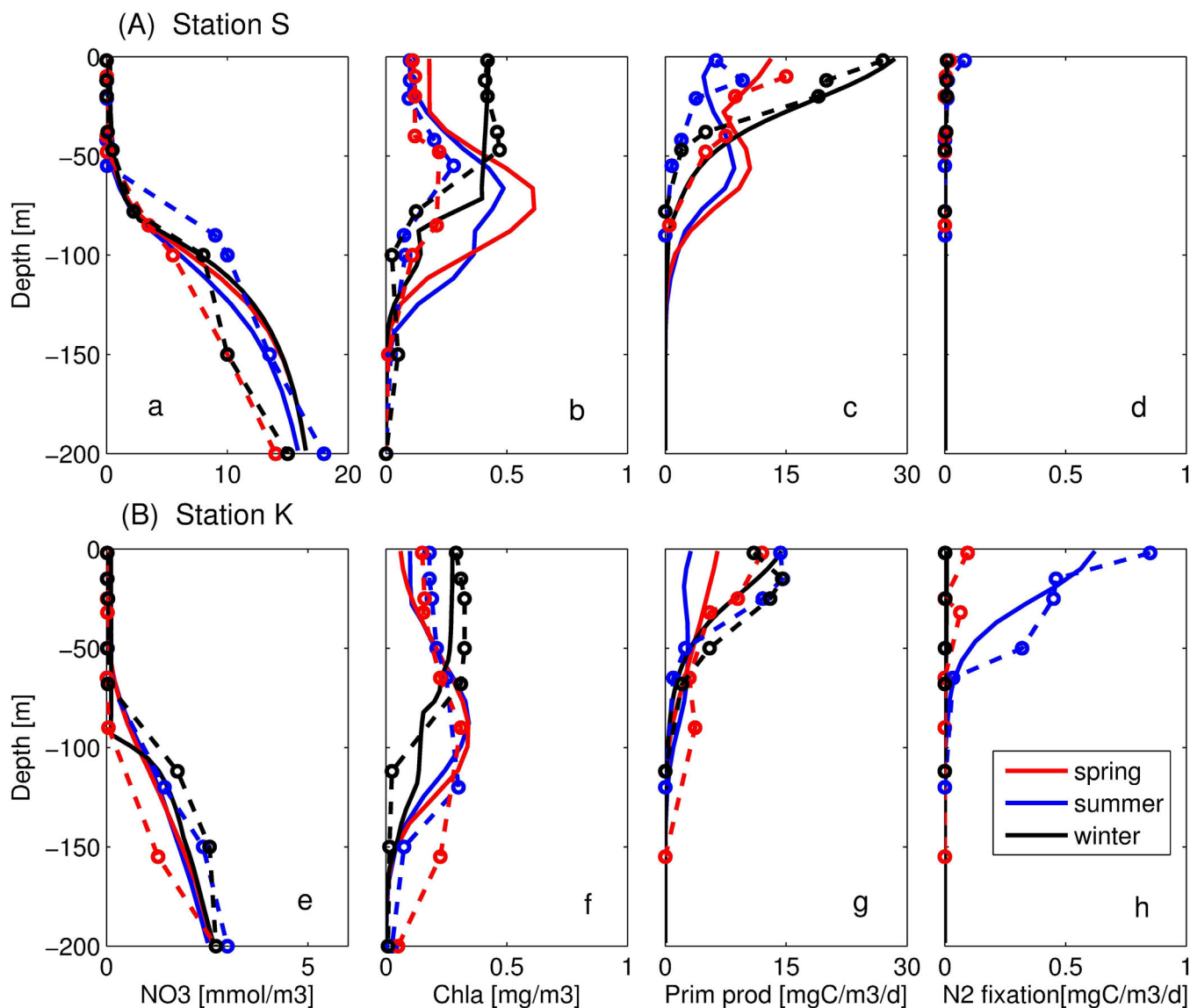


Figure 12. Comparisons of seasonal distributions of nitrate (NO_3), chlorophyll- a ($Chla$), primary production ($Pprd$), and N_2 -fixation ($Nfix$) between observations (red lines) and modeled results (blue lines) for station S (a, b, c, d) and station K (e, f, g, h). Squares are for spring, with circles for summer and diamonds for winter. Data were reproduced from Chen et al. [2008].

depth of ~ 70 m in station S during the summer of 2009, contributed by both vertical mixing (~ 1.3 mmolN/m²/d) and local upwelling (~ 1.0 mmolN/m²/d), had led to a substantially high new production of ~ 2.3 mmolN/m²/d in the model (Figure 14a) assuming a C:N ratio of 6.625, which was followed by much higher concentrations of phytoplankton, zooplankton, and exported detritus compared to that of the previous years. Interestingly, the subsurface nitrate fluxes during the summer were extremely low in station K (0.11 ± 0.04 mmolN/m²/d) when compared to that in the NSCS. The low nitrate fluxes in the summer of station K were accompanied by high diazotroph biomass and high rate of N_2 fixation (Figure 15b). This was because the physical transport of nitrate alone was not able to support the summer new production (0.71 ± 0.06 mmolN/m²/d) without the contribution of diazotroph N_2 fixation (0.64 ± 0.05 mmolN/m²/d) within the upper 50 m. Our results suggested that diazotroph community structure and N_2 fixation in the NSCS and the KC could be strongly influenced by physical processes through their impacts on vertical nutrient fluxes.

3.6. What Limits the Growth of Diazotrophs in the NSCS But Not in the KC?

The surface waters of the central NSCS and the upstream KC were characterized by high temperature, low nutrients, high stratification, and high atmospheric iron input [Liu et al., 2002; Wu et al., 2003], which

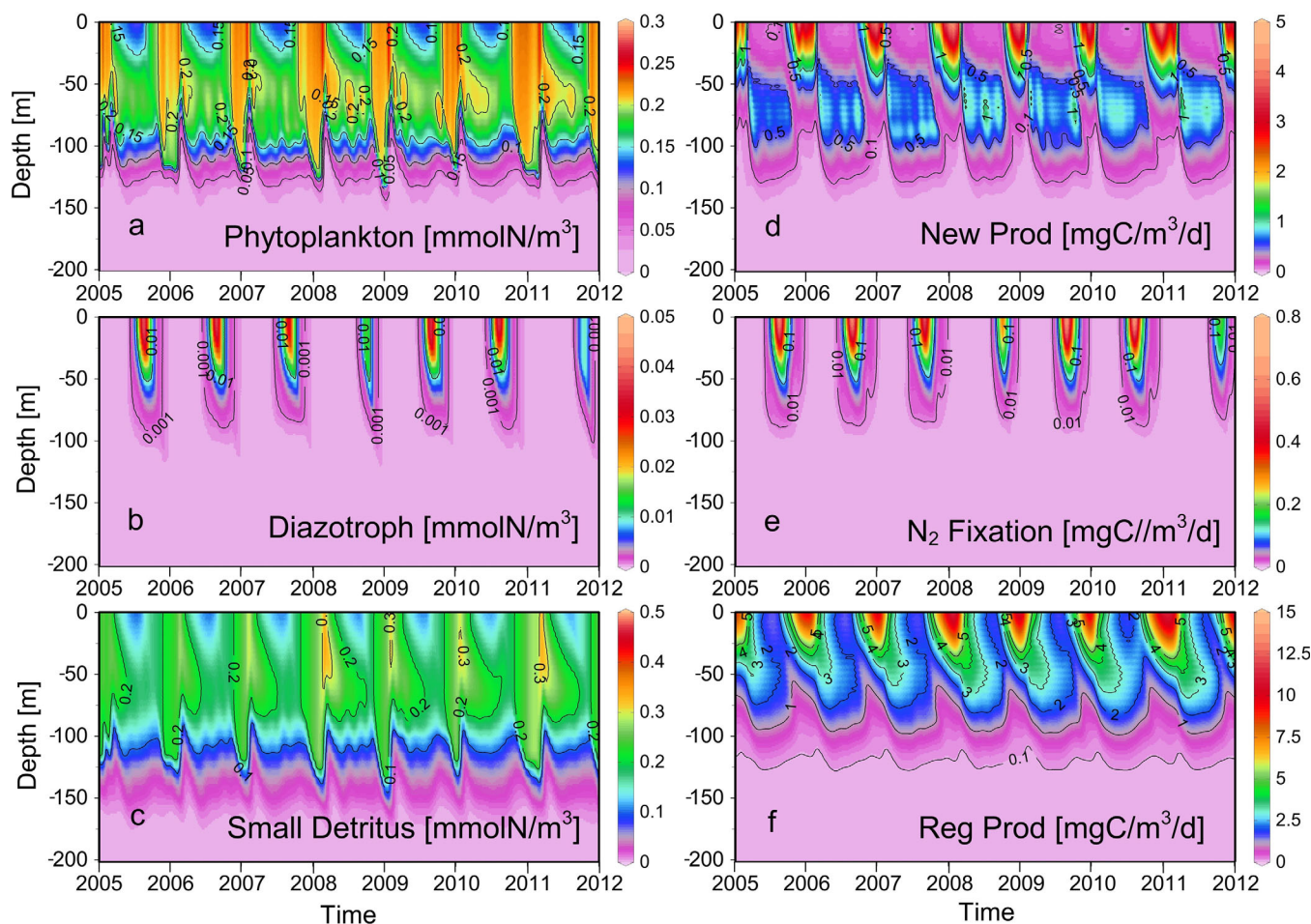


Figure 13. Time-series distributions of modeled phytoplankton (a), diazotroph (b), small detritus (c), new production (d), nitrogen fixation (e), and regeneration production (f) for station K from 2005 to 2012.

were expected to be perfect for the growth of diazotrophs as to alleviate the community nitrogen limitation by providing additional new nitrogen into the system. However, both the observations and model predictions suggested that diazotroph biomass and N_2 fixation were low in the NSCS but very high in the KC, particularly during the summer. An interesting question is what actually limits the N_2 fixation of the NSCS but not of the KC? Temperature was one of the most important factors for seasonal variations of diazotrophs in the ocean [Church *et al.*, 2009]. The temperature of the upper water column of the NSCS during the summer was always between 25°C and 30°C , falling within the optimal temperature range for *Trichodesmium* growth [Chen *et al.*, 2008]. There were not much difference for phosphate

Table 2. Seasonal Mean and Standard Deviation of Depth-Integrated Primary Production (Pprd, $\text{g C m}^{-2} \text{d}^{-1}$), Nitrate-Uptake-Based New Production (Nprd, $\text{g C m}^{-2} \text{d}^{-1}$), and *Trichodesmium* Nitrogen Fixation (Nfix, $\mu\text{mol N m}^{-2} \text{d}^{-1}$) From Model Predictions and Observations in the NSCS and the KC From 2002 to 2007^a

	SCS				KC		
	Spring	Summer	Autumn	Winter	Spring	Summer	Winter
Pprd(model)	0.58 ± 0.08	0.44 ± 0.06	0.53 ± 0.09	0.75 ± 0.04	0.45 ± 0.04	0.30 ± 0.02	0.51 ± 0.04
Pprd(obs)	0.50 ± 0.10	0.36 ± 0.08	0.54 ± 0.09	0.62 ± 0.07	0.54 ± 0.10	0.51 ± 0.06	0.53 ± 0.15
Nprd(model)	0.19 ± 0.04	0.14 (0.06)	0.26 ± 0.09	0.23 ± 0.03	0.11 ± 0.02	0.10 ± 0.04	0.18 ± 0.04
Nprd(obs)	0.21 ± 0.09	0.08 ± 0.01	0.25 ± 0.14	0.23 ± 0.04	0.14 ± 0.03	0.16 ± 0.03	0.27 ± 0.08
Nfix(model)	<DL	<DL	<DL	<DL	20 ± 11	171 ± 93	12 ± 6
Nfix(obs)	<DL	13 ± 6	<DL	<DL	35 ± 11	168 ± 167	<DL

^aObservation data reproduced from Chen *et al.* [2008]; DL is the detection limit of depth-integrated Nfix ($8 \mu\text{mol N m}^{-2} \text{d}^{-1}$), estimated based on Montoya *et al.* [1996] assuming an averaged PN of $0.3 \text{ mmol N m}^{-3}$ within the upper 120 m [Kao *et al.*, 2012].

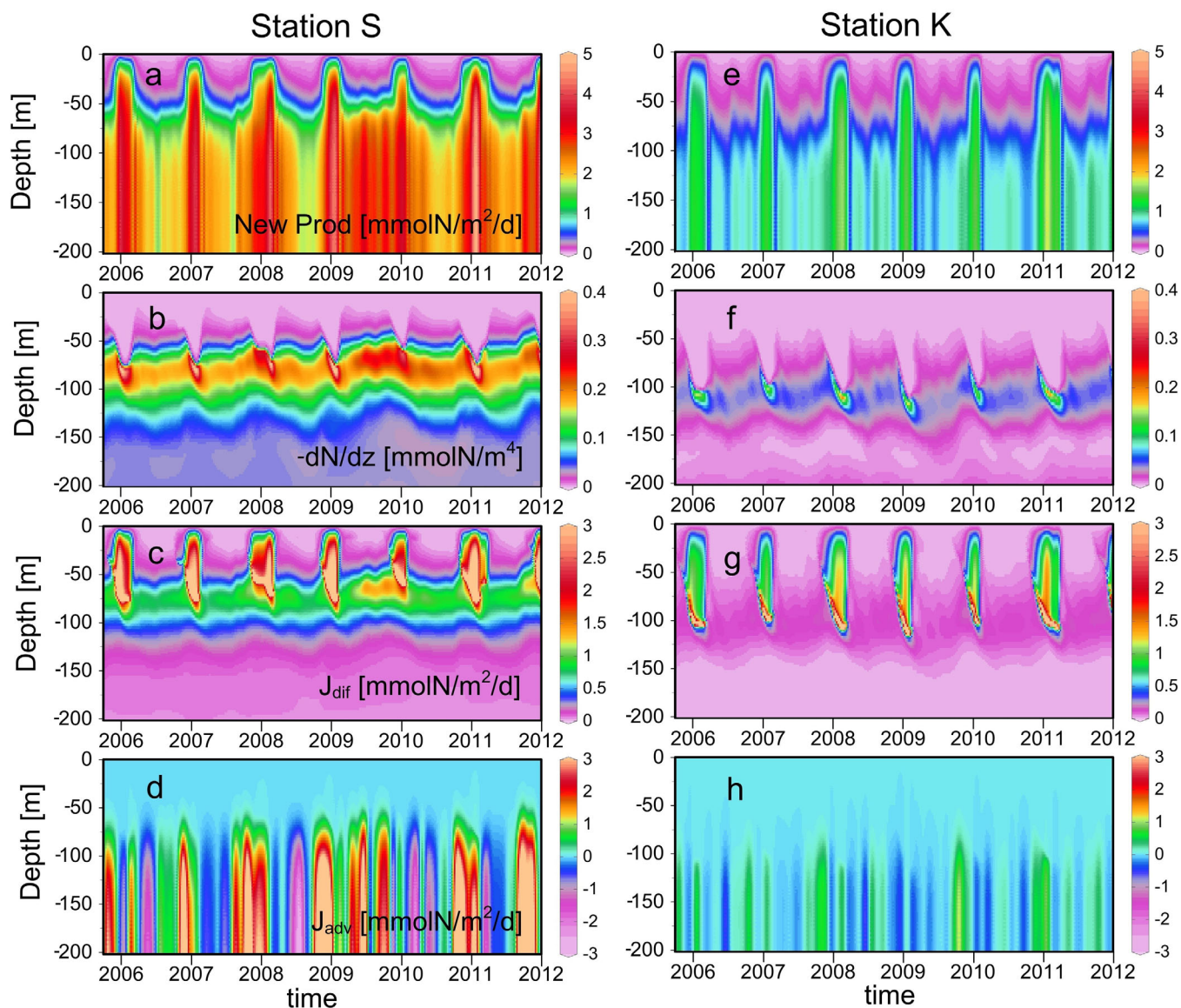


Figure 14. Time-series distributions of integrated new production (a, e), nitrate gradients $-dN/dz$ (b, f), diffusive nitrate fluxes J_{dif} (c, g), and advective nitrate fluxes J_{adv} (d, h) in stations S and K.

concentrations ($\sim 0.01 \mu\text{M}$) within the mixed layer between the NSCS and the KC during the summer, though large discrepancies were reported for phytoplankton biomass, community structure, and primary production. Furthermore, bioassay experiments near station S suggested generally nitrogen limitation but not phosphorus limitation of primary production during the spring and the summer [Wu *et al.*, 2003; Chen *et al.*, 2005]. Iron may limit the growth of N_2 -fixing organisms in remote oligotrophic regions such as the Sargasso Sea. The lack of iron-binding organic ligands in the dust rich NSCS had been proposed as a possible explanation for low *Trichodesmium* abundance and N_2 fixation rate in the regions [Wu *et al.*, 2003]. However, our results showed less favorable for the hypothesis of iron limitation of N_2 fixation in the NSCS, as the modeled diazotrophs did not thrive in the NSCS even without iron-limitation in the model.

One of the possible explanations for the disadvantage of diazotrophs in the NSCS might be the grazing impact, as higher zooplankton abundance was generally reported in the NSCS relative to the KC [Hwang *et al.*, 2007]. While the transfer of *Trichodesmium* biomass to higher trophic levels was still not well understood, existing evidences suggested that *Trichodesmium* was less favorable for grazing by many of the dominant zooplankton in the ocean [Mulholland, 2007]. It was also suggested that higher standing crop of *Trichodesmium* in the KC than the NSCS might be related to the deeper nitracline of the Kuroshio

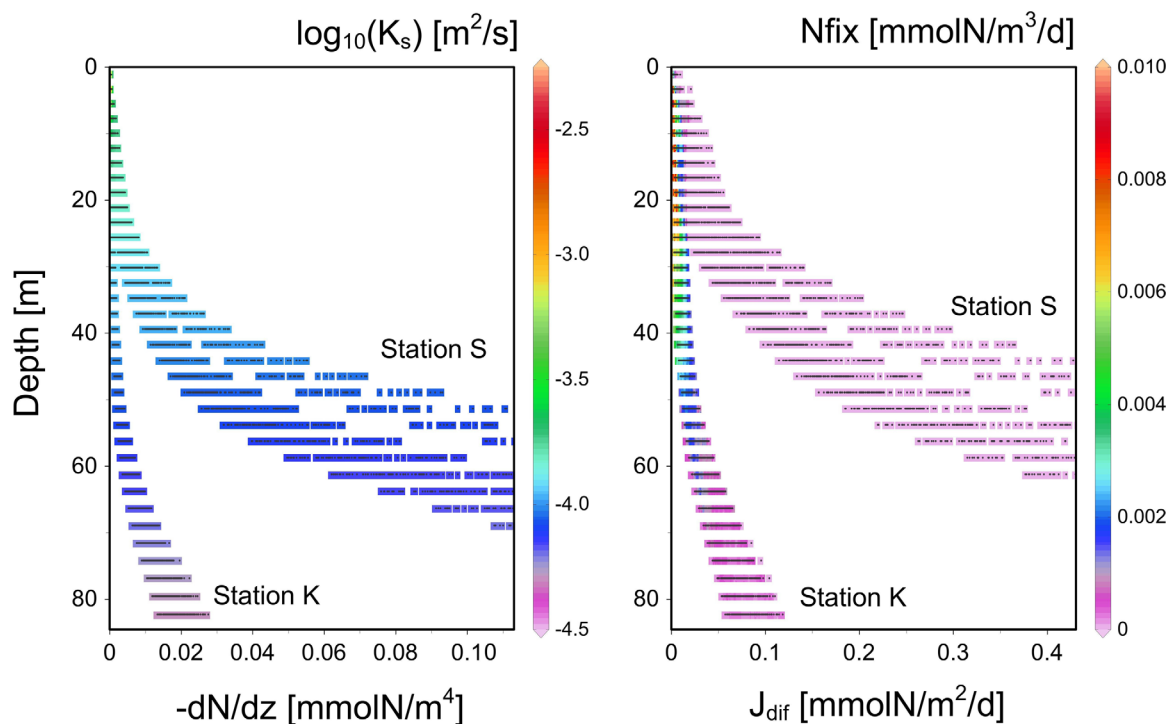


Figure 15. Comparisons of the vertical profiles of nitrate gradient $-dN/dz$ (a) and diffusive nitrate fluxes J_{dif} (b) during the summer between stations S and K. Colors show the contour of vertical diffusive coefficient $\log_{10}K_s$ (a) and nitrogen fixation rates N_{fix} (b).

[Chen *et al.*, 2008], which would result in decrease of nitrate availability, a condition favorable for diazotroph growth. However, the nitracline depth of the central NSCS during the summer was about 60 m, which was only 10–20 m shallower than that in the KC (Figures 12a and 12e). High rates of N_2 -fixation with nitracline shallower than 50 m had been observed in the offshore extension zones of the Vietnamese upwelling in the southern South China Sea [Bombar *et al.*, 2010]. Our results suggested that the low diazotroph biomass and nitrogen fixation rate in the central NSCS was caused by its high nitrate fluxes from subsurface (Figure 15), which have supplied plenty of nutrients for new production and thus the energy-costing N_2 -fixation became disadvantaged when diazotrophs competing for nutrients with the fast growing nondiazotroph phytoplankton. While, the vertical nitrate fluxes in the KC were very low and could not meet the need of phytoplankton community and N_2 fixation therefore became an important way of fixed nitrogen into the system.

Our simple 1-D model had neglected a number of 3-D processes potentially influencing the assessment of vertical nutrient fluxes of the SCS, such as Kuroshio intrusion, mesoscale eddies, and deep circulation. The influence of Kuroshio intrusion on vertical nutrient fluxes at station S could be relatively small, as the intrusive transports mainly flow westward along the continental slope due to geostrophy and as the horizontal nutrient gradients within the euphotic zone should be much lower than the vertical nutrient gradients. Mesoscale eddies were frequently observed in the northern SCS [Wang *et al.*, 2009], which could occur with a timescale much shorter than the monthly simulations conducted here but contribute to vertical nutrient fluxes of the open ocean via episodic eddy pumping [McGillicuddy *et al.*, 2007]. We had also neglected the influence by the SCS deep circulation [Liu *et al.*, 2002], which might introduce nutrient fluctuations of the deep water in a long-term timescale. In addition to the vertical nutrient fluxes from below, it was recently suggested that atmospheric deposition of anthropogenic nitrogen could be a significant source of nutrients for new production in the SCS [Kim *et al.*, 2014], but the contribution of dust particles to station S would be limited by the weak winds and the long distance from the source region [Wong *et al.*, 2007a]. Overall, our study is an important first step toward understanding the complex physical and biogeochemical dynamics of the NSCS. Future work may be improved by employing 3-D model simulations to take the above processes into account for better assessing the nitrogen budget and the role of nitrogen fixation in the NSCS and the KC.

4. Conclusions

In summary, as a process-oriented study to investigate planktonic ecosystems in the central NSCS and the upstream KC, we have developed a simple 1-D model to systematically examine the roles of vertical mixing and upwelling/downwelling by Ekman pumping on nutrient fluxes and plankton dynamics of the regions. The model reasonably simulated the long-term patterns of major physical and the biogeochemical variables including temperature, salinity, nutrients, chlorophyll, plankton biomass, and sinking particles of the two very contrasting ecosystems. The model also successfully reproduced the seasonal variability of primary production, new production, as well as nitrogen fixation in the two stations. Our results suggested that physical transport of nutrients above the nitracline was largely controlled by vertical turbulent mixing, while vertical advection by sporadic upwelling and downwelling was important for nutrient transports below the nitracline, which determined the vertical oscillations of isopycnal surface and the depth of nutricline.

Using the model, we found that that diazotroph community structure and N_2 fixation in the NSCS and the KC could be strongly influenced by physical processes through the impacts on vertical nutrient fluxes. The considerably lower abundance of diazotroph in the NSCS in compared to the KC could be attributed to its high nitrate fluxes from subsurface of the NSCS leading to outcompete of diazotrophs by faster growing nondiazotroph phytoplankton. High rate of N_2 fixation in the KC was, however, necessary as the vertical nitrate fluxes in the KC were too low to meet the need of phytoplankton community. We believe that the finding presented here will improve our understanding of nutrient dynamics and carbon cycle of the NSCS and the KC. It will be also helpful for better assessing the ecosystem responses to long-term physical forcing and climate change in the ocean.

Appendix A: Definition of Variables and their Units for the One Dimensional Model

The one-dimensional model has been forced by surface bulk fluxes and wind stress curls to reproduce the long-term variations of physical and biogeochemical properties as well as biological rates in the northern South China Sea and the upstream Kuroshio (see Table A1 for detail variables and terms included in the model).

Table A1. List of Variables in the 1-D Model

Variables	Symbol	Unit
Velocity vectors	u, v, w	$m\ s^{-1}$
Temperature	T	$^{\circ}C$
Salinity	S	‰
Ekman pumping velocity	w_e	$m\ s^{-1}$
Wind speed at 10m height	W_{10}	$m\ s^{-1}$
Net shortwave radiations	$NSWRS$	$w\ m^{-2}$
Net longwave radiations	$NLWRS$	$w\ m^{-2}$
Sea-level air temperatures	SAT	$^{\circ}C$
specific humidity	$Shum$	‰
Precipitation rates	$Prate$	$cm\ d^{-1}$
Nitrate	N_n	$mmol\ m^{-3}$
Ammonium	N_a	$mmol\ m^{-3}$
Phosphate	N^P	$mmol\ m^{-3}$
Phytoplankton	P_1	$mmol\ N\ m^{-3}$
Diazotroph	P_2	$mmol\ N\ m^{-3}$
Zooplankton	Z	$mmol\ N\ m^{-3}$
Small detritus	D_s	$mmol\ N\ m^{-3}$
Large detritus	D_L	$mmol\ N\ m^{-3}$
particulate nitrogen	PN	$mmol\ N\ m^{-3}$
Primary production	<i>Prim Prod</i>	$mg\ C\ m^{-3}\ d^{-1}$
New production	<i>New Prod</i>	$mg\ C\ m^{-3}\ d^{-1}$
Regeneration production	<i>Reg Prod</i>	$mg\ C\ m^{-3}\ d^{-1}$
N_2 -fixation-based new production	$N_2\ fixation$	$mg\ C\ m^{-3}\ d^{-1}$
diffusive nitrate fluxes	J_{dif}	$mmol\ N\ m^{-3}\ d^{-1}$
advective nitrate fluxes	J_{adv}	$mmol\ N\ m^{-3}\ d^{-1}$
Photosynthetically available radiation	PAR	$w\ m^{-2}$
Chlorophyll- <i>a</i> to carbon ratios for phytoplankton	θ^1	$mg\ Chl\ a\ (mg\ C)^{-1}$
Chlorophyll- <i>a</i> to carbon ratios for diazotroph	θ^2	$mg\ Chl\ a\ (mg\ C)^{-1}$
Sea surface temperature	SST	$^{\circ}C$
Sea surface chlorophyll- <i>a</i>	$SSChl\ a$	$mg\ m^{-3}$

Acknowledgments

This work is supported by a grant from the National One-Thousand Talent Program to Q.P.L. We would like to thank our colleagues for helps during the field studies. The data used in this paper are available on request (contact Dr. Q.P. Li at qianli@scsio.ac.cn).

References

- Bombar, D., J. W. Dippner, H. N. Doan, L. N. Ngoc, I. Liskow, N. Loick-Wilde, and M. Voss (2010), Sources of new nitrogen in the Vietnamese upwelling region of the South China Sea, *J. Geophys. Res.*, *115*, C06018, doi:10.1029/2008JC005154.
- Chai, F., et al. (2009), Seasonal and interannual variability of carbon cycle in South China Sea: A three-dimensional physical-biogeochemical modeling study, *J. Oceanogr.*, *65*(5), 703–720.
- Chen, Y. L. (2005), Spatial and seasonal variations of nitrate-based new production and primary production in the South China Sea, *Deep Sea Res., Part I*, *52*(2), 319–340, doi:10.1016/j.dsr.2004.11.001.
- Chen, Y. L., H. Y. Chen, S. Tuo, and K. Ohki (2008), Seasonal dynamics of new production from Trichodesmium N₂ fixation and nitrate uptake in the upstream Kuroshio and South China Sea basin, *Limnol. Oceanogr.*, *53*(5), 1705–1721.
- Chifflet, M., V. Andersen, L. Prieur, and I. Dekeyser (2001), One-dimensional model of short-term dynamics of the pelagic ecosystem in the NW Mediterranean Sea: Effects of wind events, *J. Mar. Syst.*, *30*, 89–114.
- Church, M. J., C. Mahaffey, R. M. Letelier, R. Lukas, J. P. Zehr, and D. M. Karl (2009), Physical forcing of nitrogen fixation diazotroph community structure in the North Pacific subtropical gyre, *Global Biogeochem. Cycle*, *23*, GB2020, doi:10.1029/2008GB003418.
- Dai, M., et al. (2009), Excess total organic carbon in the intermediate water of the South China Sea and its export to the North Pacific, *Geochim. Geophys. Geosyst.*, *10*, Q12002, doi:10.1029/2009GC002752.
- Eppley, R. W. (1972), Temperature and phytoplankton growth in sea, *Fish B-NOA*, *70*(4), 1063–1085.
- Fairall, C. W., E. F. Bradley, D. P. Rogers, J. B. Edson, and G. S. Young (1996), Bulk parameterization of air-sea fluxes for tropical ocean-global atmosphere coupled-ocean atmosphere response experiment, *J. Geophys. Res.*, *101*, 3747–3764.
- Farris, A., and M. Wimbush (1996), Wind-induced intrusion into the South China Sea, *J. Oceanogr.*, *52*, 771–784.
- Fasham, M. J. R., H. W. Ducklow, and S. M. McKelvie (1990), A nitrogen-based model of plankton dynamics in the oceanic mixed layer, *J. Mar. Res.*, *48*, 591–639.
- Fennel, K., et al. (2002), A deterministic model for N₂ fixation at stn. ALOHA in the subtropical North Pacific Ocean [J], *Deep Sea Res., Part II*, *2*(49): 149–174.
- Gan, J., Y. Cheung, X. Guo, and L. Li (2009), Intensified upwelling over a widened shelf in the northeastern South China Sea, *J. Geophys. Res.*, *114*, C09019, doi:10.1029/2007JC004660.
- Gan, J., Z. Lu, M. Dai, A. Cheung, H. Liu, and P. Harrison (2010), Biological response to intensified upwelling and to a river plume in the northeastern South China Sea: A modeling study, *J. Geophys. Res.*, *115*, C09001, doi:10.1029/2009JC005569.
- Gill, A.E. (1982), *Atmosphere-Ocean Dynamics*, *Int. Geophys. Ser.*, vol. 30, Academic, London, U. K.
- Gruber, N., H. Frenzel, S. C. Doney, P. Marchesiello, J. C. McWilliams, J. R. Moisan, J. J. Oram, G. H. Plattner, and K. D. Stolzenbach (2006), Eddy-resolving simulation of plankton ecosystem dynamics in the California Current System, *Deep Sea Res., Part I*, *53*, 1483–1516.
- Hood, R. R., N. R. Bates, D. G. Capone, and D. B. Olson (2001), Modeling the effect of nitrogen fixation on carbon and nitrogen fluxes at BATS, *Deep Sea Res., Part II*, *48*, 1609–1648.
- Hwang, J. S., H. U. Dahms, L. C. Tseng, and Q. C. Chen (2007), Intrusions of the Kuroshio Current in the northern South China Sea affect copepod assemblages of the Luzon Strait, *J. Exp. Mar. Biol. Ecol.*, *352*, 12–27.
- Kao, S. J., J. Y. T. Yang, K. K. Liu, M. Dai, W. C. Chou, H. L. Lin, and H. Ren (2012), Isotope constraints on particulate nitrogen source and dynamics in the upper water column of the oligotrophic South China Sea, *Global Biogeochem. Cycles*, *26*, GB2033, doi:10.1029/2011GB004091.
- Kim, T. K., K. Lee, R. Duce, and P. Liss (2014), Impact of atmospheric nitrogen deposition on phytoplankton productivity in the South China Sea, *Geophys. Res. Lett.*, *41*(9), 3156–3162.
- Large, W. G., J. C. McWilliams, and S. C. Doney (1994), Oceanic vertical mixing: A review and a model with a nonlocal boundary layer parameterization, *Rev. Geophys.*, *32*, 363–403.
- Ledwell, J. R., D. J. McGillicuddy, and L. A. Anderson (2008), Nutrient flux into an intense deep chlorophyll layer in a mode-water eddy, *Deep-Sea Res., Part II*, *55*, 1139–1160.
- Li, C. H., X. P. Jia, and W. G. Cai (2004), Diversity of marine zooplankton in the north of South China Sea, *J. Fish. Sci. China*, *11*(2), 139–146.
- Li, Q. P., and D. A. Hansell (2008), Nutrient distribution in baroclinic eddies of the oligotrophic North Atlantic and inferred impacts on biology, *Deep Sea Res., Part II*, *55*, 1291–1299.
- Li, Q. P., P. J. S. Franks, M. R. Landry, R. Goericke, and A. G. Taylor (2010), Modeling phytoplankton growth rates and chlorophyll to carbon ratios in California coastal and pelagic ecosystems, *J. Geophys. Res.*, *115*, G04003, doi:10.1029/2009JG001111.
- Li, Q. P., P. J. S. Franks, M. D. Ohman, and M. R. Landry (2012), Enhanced nitrate flux and biological processes in a frontal zone of the California Current System, *J. Plankton Res.*, *34*, 790–801.
- Lin, I., et al. (2003), New evidence for enhanced ocean primary production triggered by tropical cyclone, *Geophys. Res. Letters*, *30*(13), 1718, doi:10.1029/2003GL017141.
- Liu, H., J. Chang, C. M. Tseng, L. S. Wen, and K. K. Liu (2007), Seasonal variability of picoplankton in the Northern South China Sea at the SEATS station, *Deep Sea Res., Part II*, *54*, 1602–1616.
- Liu, K. K., S. Y. Chao, P. T. Shaw, G. C. Gong, C. C. Chen, and T. Y. Tang (2002), Monsoon-forced chlorophyll distribution and primary production in the South China Sea: Observations and a numerical study, *Deep Sea Res., Part I*, *49*(8), 1387–1412.
- Liu, K. K., et al. (2013), Inter-annual variation of chlorophyll in the northern South China Sea observed at the SEATS Station and its asymmetric responses to climate oscillation, *Biogeosciences*, *10*(11), 7449–7462, doi:10.5194/bg-10-7449-2013.
- Lu, Z., J. Gan, and M. Dai (2011), Modeling seasonal and diurnal pCO₂ variations in the northern South China Sea, *J. Mar. Syst.*, *92*(1), 30–41, doi:10.1016/j.jmarsys.2011.10.003.
- Macias, D., P. J. S. Franks, M. D. Ohman, and M. R. Landry (2012), Modeling the effects of coastal wind and wind stress curl driven upwellings on plankton dynamics in the Southern California Current system, *J. Mar. Syst.*, *94*, 107–119.
- Maes, C., J. Picaut, and S. Sophie Belamari (2005), Importance of the salinity barrier layer for the buildup of El Niño, *J. Clim.*, *18*, 104–118.
- McGillicuddy, D. J., et al. (2007), Eddy-wind interactions stimulate extraordinary mid-ocean plankton blooms, *Science*, *316*, 1021–1026.
- Metzger, E. J. (2003), Upper ocean sensitivity to wind forcing in the South China Sea, *J. Oceanogr.*, *59*, 783–798.
- Montoya, J. P., M. Voss, P. Kaehler, and D. G. Capone (1996), A simple, high precision tracer assay for dinitrogen fixation, *Appl. Environ. Microbiol.*, *62*, 986–993.
- Mulholland, M. R. (2007), The fate of nitrogen fixed by diazotrophs in the ocean, *Biogeosciences*, *4*, 37–51.
- Ryckaczewski, R. R., and D. M. Checkley (2008), Influence of ocean winds on the pelagic ecosystem in upwelling regions, *Proc. Natl. Acad. Sci. U. S. A.*, *105*(6), 1065–1070.

- Shang, S. L., Q. Dong, C. M. Hu, G. Lin, Y. H. Li, and S. P. Shang (2014), On the consistency of MODIS chlorophyll a products in the northern South China Sea, *Biogeosciences*, *11*, 269–280.
- Shchepetkin, A., and J. C. McWilliams (2005), The regional oceanic modeling system: A split-explicit, free-surface, topography following-coordinate ocean model, *Ocean Modell.*, *9*, 347–404.
- Song, X., X. Liu, L. Huang, Y. Tan, Z. Ke, and L. Zhou (2010), Distribution characteristics of basic biological production and its influencing factors in the northern South China Sea in summer. *Acta Ecol. Sin.*, *30*(23), 6409–6417.
- Taylor, K. E. (2000), Summarizing multiple aspects of model performance in a single diagram, *J. Geophys. Res.*, *106*, 7183–7192.
- Tian, J., Q. Yang, X. Liang, L. Xie, X. Hu, F. Wang, and T. D. Qu (2006), Observation of Luzon Strait transport, *Geophys. Res. Letter*, *33*, L19607, doi:10.1029/2006GL026272.
- Tseng, C. M., G. T. F. Wong, I. I. Lin, C. R. Wu, and K. K. Liu (2005), A unique seasonal pattern in phytoplankton biomass in low-latitude waters in the South China Sea, *Geophys. Res. Letter*, *32*, L08608, doi:10.1029/2004GL022111.
- Troupin, C., P. Sangra, and J. Aristegui (2010), Seasonal variability of the oceanic upper layer and its modulation of biological cycles in the Canary Island region, *J. Mar. Syst.*, *80*(3–4), 172–183.
- Wang, D., Y. Deng, and W. Wang (2009), Research progress in the South China Sea circulation and local air-sea interaction during 2003–2006, *Adv. Geosci.*, *12*, 145–160.
- Wang, J., and D. Tang (2014), Phytoplankton patchiness during spring intermonsoon in west coast of South China Sea, *Deep Sea Res., Part II*, *101*, 120–128.
- Wong, G. T. F., T. L. Ku, M. Mulholland, C. M. Tseng, and D. P. Wang (2007a), The South East Asian Time-series Study (SEATS) and the biogeochemistry of the South China Sea: An overview, *Deep Sea Res., Part II*, *54*, 1434–1447.
- Wong, G. T. F., C. M. Tseng, L. S. Wen, and S. W. Chung (2007b), Nutrient dynamics and N-anomaly at the SEATS station, *Deep Sea Res., Part II*, *54*, 1528–1545.
- Wu, J. F., S. W. Chung, L. S. Wen, K. K. Liu, Y. L. L. Chen, H. Y. Chen, and D. M. Karl (2003), Dissolved inorganic phosphorus, dissolved iron, and Trichodesmium in the oligotrophic South China Sea, *Global Biogeochemical Cycles*, *17*(1), 1008, doi:10.1029/2002GB001924.
- Xie, S. P., Q. Xie, D. X. Wang, and W. T. Liu (2003), Summer upwelling in the South China Sea and its role in regional climate variations, *J. Geophys. Res.*, *108*(C8), 3261, doi:10.1029/2003JC001867.
- Xu, J., K. Yin, L. He, X. Yuan, A. Y. T. Ho, and P. J. Harrison (2008), Phosphorus limitation in the northern South China Sea during late summer: Influence of the Pearl River, *Deep Sea Res., Part I*, *55*(10), 1330–1342.